Chapter 6
Electronic Surface States

Since the surface is the termination of a bulk crystal, surface atoms have fewer neighbors than bulk atoms; part of the chemical bonds which constitute the bulk-crystal structure are broken at the surface. These bonds have to be broken to create the surface and thus the formation of a surface costs energy (*surface energy*) (Sect. 3.1). In comparison with the bulk properties, therefore, the electronic structure near to the surface is markedly different. Even an ideal surface with its atoms at bulk-like positions (called *truncated bulk*) displays new electronic levels and modified many-body effects due to the change in chemical bonding. Many macroscopic effects and phenomena on surfaces are related to this change in electronic structure, for example, the surface free energy, the adhesion forces, and the specific chemical reactivity of particular surfaces. A central topic in modern surface physics is therefore the development of a detailed understanding of the surface electronic structure. On the theoretical side, the general approach is similar to that for the bulk crystal: In essence the one-electron approximation is used and one tries to solve the Schrödinger equation for an electron near the surface. A variety of approximation methods may then be used to take into account many-body effects.

In comparison with the bulk problem two major difficulties arise for the surface. Even in the ideal case translational symmetry only exists in directions within the plane of the surface. Perpendicular to the surface the periodicity breaks down and the mathematical formalism becomes much more complicated. Even more severe, and not generally solved up to now, is the surface-structure problem. A complete calculation of the electronic structure requires a knowledge of the atomic positions (coordinates). Because of the changed chemical bonding near the surface, however, surface relaxations and reconstructions frequently occur. This means that the atoms are displaced from the ideal positions which they would occupy if the bulk crystal were simply truncated into two parts. At present there is no general, simple and straightforward experimental technique to determine the atomic structure in the topmost atomic layers. Several relatively complex methods such as dynamic LEED analysis (Sect. 4.4), SEXAFS (Panel VII: Chap. 3), STM (Panel VI: Chap. 3), and atom scattering (Panel X: Chap. 5) give some information, but only relatively few structures, e.g. the GaAs(110) and the Si(111) surface (Sect. 3.2) have actually been accurately established. It is interesting to mention, that in the case of the Si(111)-(7 $\times$ 7) the main contribution was obtained by means of transmission

H. Lüth, *Solid Surfaces, Interfaces and Thin Films*, 5th ed., Graduate Texts in Physics,
DOI 10.1007/978-3-642-13592-7_6,

electron microscopy using simple kinematic analysis. A break through for the analysis of surface atomic structure has been achieved recently by scanning electron tunneling microscopy [6.1] (Panel VI: Chap. 3).

For realistic calculations of the electronic structure of surfaces one thus has to assume structural models and then to compare the calculated surface electronic band structure and other calculated physical properties, e.g. photoemission and electron energy loss spectra, with experiment.

In the following, we will first consider a simple (unrealistic) model of a surface, namely the monatomic linear chain terminated at one end (semi-infinite chain). The Schrödinger equation will be solved in the nearly-free-electron approximation and the results transferred qualitatively to the case of a real, two-dimensional (2D) surface with 2D translational symmetry. Realistic surfaces and surface states of some metals, and important semiconductors such as Si and GaAs are discussed afterwards.

6.1 Surface States for a Semi-Infinite Chain in the Nearly-Free Electron Model

If we want to make simple-model calculations of the electronic surface states on a crystalline surface, we are faced with a situation similar to that encountered in the case of surface phonons (Chap. 5). Within the surface plane we have to assume the ideal 2D periodicity. In the perpendicular direction, however, the translational symmetry is broken at the surface. Thus the most general one-electron wavefunction ϕ_{ss} for states localized near an ideal surface has plane-wave (Block) character for co-ordinates parallel to the surface $\boldsymbol{r}_\parallel = (x, y)$:

$$\phi_{ss}(\boldsymbol{r}_\parallel, z) = u_{\boldsymbol{k}_\parallel}(\boldsymbol{r}_\parallel, z) \exp(\mathrm{i}\boldsymbol{k}_\parallel \cdot \boldsymbol{r}_\parallel), \tag{6.1}$$

where $\boldsymbol{k}_\parallel = (k_x, k_y)$ is a wave vector parallel to the surface. The modulation function $u_{\boldsymbol{k}_\parallel}$ has the periodicity of the surface and is labelled according to the wave vector $\boldsymbol{k}_\parallel$. If one were to neglect the variation of the crystal potential parallel to the surface, $u_{\boldsymbol{k}_\parallel}(z)$ would not depend on $\boldsymbol{r}_\parallel$. Because of the 3D translational symmetry in the bulk one can take as the simplest model a semi-infinite chain of identical, periodically arranged atoms. The end of the chain then represents the surface. As in the phonon problem one can use this model to derive the essential properties of surface states, and can then readily generalize the results to the 2D surface of an ideal crystal. In the sense of the nearly-free electron model, we assume a cosine variation of the potential along the chain (Fig. 6.1)

$$V(z) = \hat{V}\left[\exp\left(\frac{2\pi \mathrm{i}z}{a}\right) + \exp\left(\frac{-2\pi \mathrm{i}z}{a}\right)\right] = 2\hat{V}\cos\left(\frac{2\pi z}{a}\right), \quad \text{for } z < 0. \tag{6.2}$$

The surface ($z = 0$) is modelled by an abrupt potential step V_0 which is certainly an oversimplification for any realistic surface.

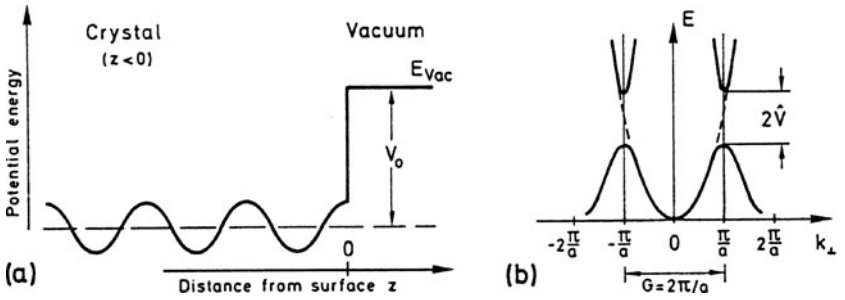

Fig. 6.1 a,b Nearly-free-electron model for a cosine potential along a linear chain (z-direction). (**a**) Potential energy in the presence of a surface at $z = 0$. (**b**) Energy bands $E\,(k_\perp)$ for one-electron bulk states

We now try to solve the Schrödinger equation

$$\left[-\frac{\hbar^2}{2m}\frac{\mathrm{d}^2}{\mathrm{d}z^2} + V(z)\right]\psi(z) = E\psi(z) \tag{6.3}$$

using the potential (6.2) for $V(z)$.

We start from regions "deep inside the crystal", i.e. at locations $z \ll 0$ far away from the surface $z = 0$. In this region one can consider the chain as effectively infinite and neglect surface effects. The potential $V(z)$ can be assumed to be periodic, $V(z) = V(z + na)$, and the well-known bulk solutions, as described in every elementary solid-state physics textbook, e.g. [6.2], are obtained. Away from the Brillouin zone boundaries $k_\perp = \pm\pi/a$ ($k_\perp$ is wave vector normal to the surface) the electronic states have plane-wave character and their energies are those of the free electron parabola (Fig. 6.1b). Near to the zone boundaries the characteristic band splitting occurs. This arises from the fact that the electronic wave function must now be taken in the lowest-order approximation, as a superposition of two plane waves. At the zone boundary an electron is scattered from a state $k_\perp = \pi/a$ into a state $k_\perp = -\pi/a$. For $k_\perp$ values near $\pi/a = G/2$ (G is reciprocal lattice vector) one therefore has in this two-wave approximation:

$$\psi(z) = A\mathrm{e}^{\mathrm{i}k_\perp z} + B\mathrm{e}^{\{\mathrm{i}[k_\perp - (2\pi/a)]z\}}. \tag{6.4}$$

Using the potential (6.2) and substituting (6.4) into the Schrödinger equation (6.3) yields the matrix equation

$$\begin{pmatrix} \frac{\hbar^2}{2m}k_\perp^2 - E(k_\perp) & \hat{V} \\ \hat{V} & \frac{\hbar^2}{2m}\left(k_\perp - \frac{2\pi}{a}\right)^2 - E(k_\perp) \end{pmatrix}\begin{pmatrix} A \\ B \end{pmatrix} = 0 \tag{6.5}$$

which is solved by setting its determinant equal to zero. We are interested in solutions around the Brillouin-zone boundary, i.e. near $k_\perp = \pm G/2 = \pm\pi/a$. With

$k_\perp = \kappa + \pi/a$, where small values of κ correspond to the interesting $k_\perp$ range, the energy eigenvalues are obtained by solving (6.5) as

$$E = \frac{\hbar^2}{2m}\left(\frac{\pi}{a} + \kappa\right)^2 \pm |\hat{V}| \left[\frac{-\hbar^2\pi\kappa}{ma|\hat{V}|} \pm \sqrt{\left(\frac{\hbar^2\pi\kappa}{ma|\hat{V}|}\right)^2 + 1}\right]. \tag{6.6}$$

The electronic wave functions ψ_i for spatial regions deep inside the interior crystal (subscript i) are obtained, for $z \ll 0$, by using (6.6), solving (6.5) for A and B and introducing the result into (6.4):

$$\psi_\mathrm{i} = C\mathrm{e}^{\mathrm{i}\kappa z}\left\{\mathrm{e}^{\mathrm{i}\pi z/a} + \frac{|\hat{V}|}{\hat{V}}\left[\frac{-\hbar^2\pi\kappa}{ma|\hat{V}|} \pm \sqrt{\left(\frac{\hbar^2\pi\kappa}{ma|\hat{V}|}\right)^2 + 1}\right]\mathrm{e}^{-\mathrm{i}\pi z/a}\right\}. \tag{6.7}$$

C is the remaining normalization constant. For regions deep inside the crystal ($z \ll 0$), the electronic energy levels form the familiar electronic bands $E(k_\perp)$ which are periodic in reciprocal $k_\perp$-space (Fig. 6.1b). The "free electron" parabola splits near the zone boundaries $k_\perp = \pm\pi/a$, and allowed and forbidden energy bands arise. The $E(k_\perp = \kappa + \pi/a)$ dependence is parabolic near $\pm\pi/a$ as is seen from (6.6), and the amount of splitting, i.e. the width of the forbidden band is $2|\hat{V}|$ according to (6.6).

Our main goal in this chapter is to look for solutions of the Schrödinger equation (6.3) near a solid surface, i.e. near the end of the chain (Fig. 6.1a, $z = 0$). These solutions must be composed of a part which is compatible with the constant potential $E_\mathrm{vac} = V_0$ on the vacuum side ($z > 0$) and of a contribution which solves the Schrödinger equation (6.3) on the crystal side with its cosine potential (6.2). The two solutions for $z > 0$ and $z < 0$ have to be matched at the surface $z = 0$. Matching is necessary both for ψ itself and its derivation $\partial\psi/\partial z$. Any solution ψ_0 in the constant potential V_0 of the vacuum side ($z > 0$) which can be normalized must be exponentially decaying

$$\psi_0 = D\exp\left[-\sqrt{\frac{2m}{\hbar^2}(V_0 - E)}\,z\right], \quad E < V_0. \tag{6.8}$$

Since (6.8) contains no complex contribution $\exp(\mathrm{i}\kappa z)$, solutions inside the crystal ψ_i of the type (6.7) can only be matched to (6.8) if a superposition of both an incoming and a reflected wave (standing wave) is taken into account. One matching condition is thus

$$\psi_0(z = 0) = \alpha\psi_\mathrm{i}(z = 0, \kappa) + \beta\psi_\mathrm{i}(z = 0, -\kappa), \tag{6.9}$$

with ψ_0 and ψ_i from (6.8) and (6.7), respectively. Equation (6.9) and the corresponding relation for the derivatives can, in fact, be fulfilled for every possible

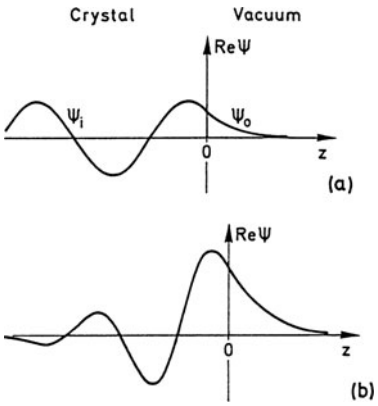

Fig. 6.2 Real part of the one-electron wavefunction, Re$\{\psi\}$, for (**a**) a standing Bloch wave (ψ_i), matched to an exponentially decaying tail (ψ_0) in the vacuum; (**b**) a surface-state wave function localized at the surface ($z = 0$)

energy eigenvalue E within the allowed band. Possible surface solutions are therefore standing Bloch waves inside the crystal which are matched to exponentially decaying tails on the vacuum side (Fig. 6.2a). The corresponding electronic energy levels are therefore only slightly modified from those of the infinite bulk crystal. The bulk electronic band structure therefore exists up to the very surface of a crystal with only slight alterations.

Additional surface solutions become possible if we allow complex wave vectors. Letting κ to be imaginary

$$\kappa = -\mathrm{i}q \tag{6.10a}$$

and defining, for convenience,

$$\gamma = \mathrm{i}\sin(2\delta) = -\mathrm{i}\frac{\hbar^2 \pi q}{ma|\hat{V}|} \tag{6.10b}$$

one can show that the energy eigenvalues (6.6) remain real for a particular range of κ, i.e. these values represent possible solutions of the Schrödinger equation. The electronic wave function for imaginary κ inside the crystal ($z < 0$) results from (6.7) by using (6.10a)

$$\psi_\mathrm{i}'(z \le 0) = \mathrm{F}\mathrm{e}^{\mathrm{q}z}\left\{\exp\left[\mathrm{i}\left(\frac{\pi}{a}z \pm \delta\right)\right] \mp \exp\left[-\mathrm{i}\left(\frac{\pi}{a}z \pm \delta\right)\right]\right\}\mathrm{e}^{\mp\mathrm{i}\delta}. \tag{6.11}$$

This is essentially a standing wave with an exponentially decaying amplitude (Fig. 6.2b). The energy eigenvalues are obtained from (6.6) with (6.9) as

$$E = \frac{\hbar^2}{2m}\left[\left(\frac{\pi}{a}\right)^2 - q^2\right] \pm |\hat{V}|\sqrt{1 - \left(\frac{\hbar^2 \pi q}{ma|\hat{V}|}\right)^2}. \tag{6.12}$$

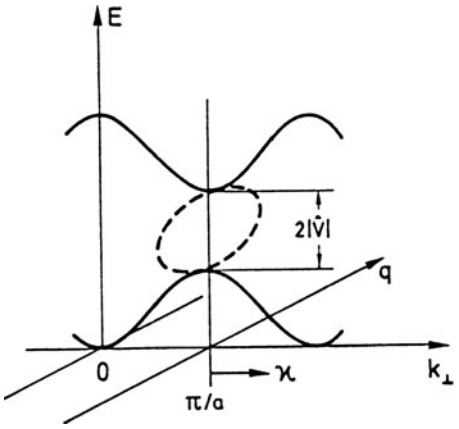

Fig. 6.3 Electronic band structure (qualitative) for a semi-infinite chain of atoms. Bulk Bloch states which are little disturbed by the presence of the surface give rise to energy bands $E(k_\perp)$ that are periodic in wave vector $k_\perp$ parallel to the chain direction, i.e. normal to the surface (solid curves). States with a wave function amplitude exponentially decaying from the surface ($z = 0$) into the bulk ($z < 0$) are found between the bulk states for complex wave vectors $\pi/a - iq$ (broken curve)

The values of E remain real (as required for energies) and ψ does not diverge for large negative z if $0 < q < q_{\max} = ma|\hat{V}|\hbar^2\pi$. In this q range the E versus q dependence is described by (6.12); all energies fall into the forbidden gap of the bulk electronic-band structure (Fig. 6.3).

Equation (6.11) is not the complete solution for a surface electronic state, since the part of the wave function on the vacuum side, $z > 0$ is missing. To obtain the complete solution for our surface problem, we have to match the wave functions (6.11) to the exponentially decaying vacuum solution (6.8). The matching conditions require for the wave functions and for their derivatives:

$$\psi_0(z=0) = \psi_i'(z=0) \text{ and } \left.\frac{d\psi_0}{dz}\right|_{z=0} = \left.\frac{d\psi_i'}{dz}\right|_{z=0}. \tag{6.13}$$

For this matching procedure (two equations) there are exactly two free parameters which are thus fixed by (6.13): the energy eigenvalue E and the ratio D/F of the wave-function amplitudes in (6.8 and 6.11). The wave function of the resulting electronic surface state is shown qualitatively in Fig. 6.2b. Its amplitude vanishes for $\pm z$ values far away from the surface. Electrons in these states are, in fact, localized within a couple of Ångstroms of the surface plane. Another important consequence of the matching conditions (6.13) is the restriction on the allowed values of E. Of the continuous range of E values within the forbidden bulk energy gap (Fig. 6.3), only one single energy level E is fixed by means of the requirement (6.13). The present calculation for the semi-infinite chain therefore yields one single electronic surface state which is located somewhere in the gap of the bulk states.

6.2 Surface States of a 3D Crystal and Their Charging Character

6.2.1 Intrinsic Surface States

The generalization of the results for the one-dimensional semi-infinite chain to the 2D surface of a 3D crystal is straightforward. Because of the 2D translational symmetry parallel to the surface, the general form of a surface-state wave function is of the Bloch type (6.1) in coordinates $\boldsymbol{r}_\parallel$ parallel to the surface, i.e. the variation in $\boldsymbol{r}_\parallel$ enters through the factor $\exp(\mathrm{i}\boldsymbol{k}_\parallel \cdot \boldsymbol{r}_\parallel)$ and the energy is increased by the term $\hbar^2 k_\parallel^2/2m$. The energy eigenvalues (6.12) therefore become functions of $k_\perp = \pi/a - \mathrm{i}q$ and of the wave vector $\boldsymbol{k}_\parallel$ parallel to the surface. The matching conditions (6.13) thus have to be fulfilled for each $\boldsymbol{k}_\parallel$ separately and for each $\boldsymbol{k}_\parallel$ a single, but in general different, energy level for the surface state is obtained. We thus arrive at a 2D band structure $E_{\mathrm{ss}}(\boldsymbol{k}_\parallel)$ for the energies E_{ss} of electronic surface states. The $E_{\mathrm{ss}}(\boldsymbol{k}_\parallel)$ bands are defined in the 2D reciprocal $\boldsymbol{k}_\parallel$-space of the surface. The description is analogous to that of surface-phonon dispersion branches (Chap. 5). Since bulk electronic states are also found at the surface, with only minor modifications, one has to take them into account when mapping the true surface states.

A surface state is described by its energy level E_{ss} and its wave vector $k_\parallel$ parallel to the surface. For bulk states both $k_\parallel$ and $k_\perp$ components are allowed. For each value of $k_\parallel$ therefore, a rod of $k_\perp$ values extends back into the bulk 3D Brillouin zone; bulk energy bands being cut by this rod yield a bulk state in the $E_{\mathrm{ss}}(k_\parallel)$ plane. We thus arrive at a presentation in which surface-state bands (broken lines in Fig. 6.4) are plotted together with a projection of all bulk states (hatched area in Fig. 6.4) in a particular $E(\boldsymbol{k}_\parallel)$ plane. True surface-state bands are characterized by energy levels E_{ss} that are not degenerate with bulk bands; they lie in the gaps of the projected bulk-band structure. Surface-state bands, however, can penetrate into a part of the surface Brillouin zone, where propagating bulk states exist (short dotted lines in Fig. 6.4). They are then degenerate with bulk states and can mix with them. Such a state will propagate deep into the bulk, similar to a Bloch state with finite $k_\perp$, but will nevertheless retain a large amplitude close to the surface. These states are known as *surface resonances*.

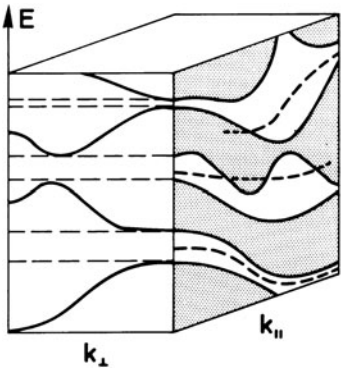

Fig. 6.4 Hypothetical electronic band structure of a crystal. The shaded areas in the $E(k_\parallel)$ plane describe the projected bulk-band structure (along $k_\perp$). Broken lines in the $E(k_\parallel)$ plane indicate surface state bands in the gaps of the projected bulkband structure, and surface resonances where they are degenerate with bulk states (short dotted lines)

The discussion of realistic surface-state bands in the next chapters is based on representations such as indicated in Fig. 6.4 where the energy levels E_{ss} are plotted along particular symmetry directions $\boldsymbol{k}_{\parallel}$ of the 2D surface Brillouin zone. For the most important crystal structures fcc, bcc, and hcp the relation of the low-index surface Brillouin zones to their bulk counterparts has already been described in connection with surface phonon dispersion (Figs. 5.5–5.7). The projections of the bulk Brillouin zones on particular surfaces are very helpful for establishing whether a particular state falls into a gap of the bulk band structure.

So far we have discussed the existence of surface states on ideal, clean surfaces in the framework of the nearly-free-electron model. For historical reasons, such surface states are often called *Schockley states* [6.3]. One can also approach the question of the existence of electronic surface states from the other limiting case of tightly bound electrons. This approximate treatment in terms of wave functions that are linear combinations of atomic eigenstates was first given by Tamm [6.4]. The resulting states are often called *Tamm states*, even though there is no real physical distinction between the different terms; only the mathematical approach is different. The existence of electronic surface states, whose energy is different from the bulk states, is qualitatively easy to see within the picture of tightly bound electrons (Linear Combination of Atomic Orbitals, LCAO). For the topmost surface atoms the bonding partners on one side are missing in total, which means that their wave functions have less overlap with wave functions of neighboring atoms. The splitting and shift of the atomic energy levels is thus smaller at the surface than in the bulk (Fig. 6.5). Every atomic orbital involved in chemical bonding and producing one

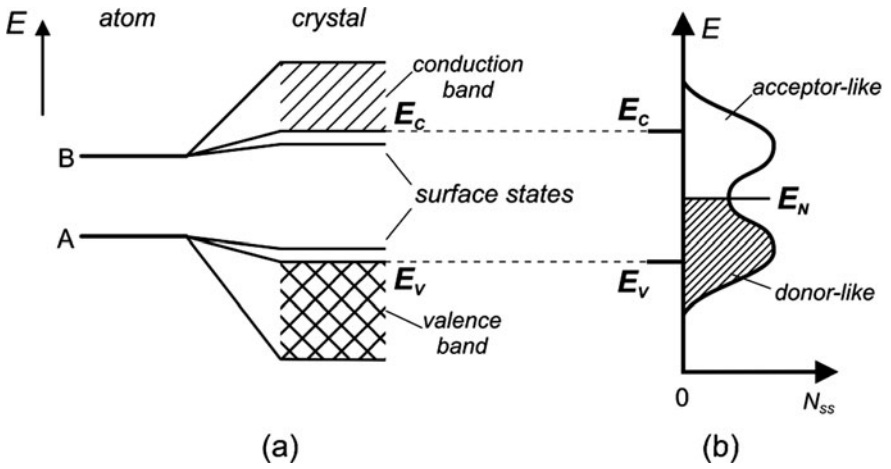

Fig. 6.5 Qualitative explanation of the origin of surface states in the tight-binding picture. (**a**) Two atomic levels A and B form the bulk valence and conduction bands, respectively. Surface atoms have fewer bonding partners than bulk atoms and thus give rise to electronic energy levels that are closer to those of the free atoms, i.e. surface state levels are split off from the bulk bands. Depending on their origin, these states have acceptor- or donor-like charging character. (**b**) Mostly these (intrinsic) surface states having the periodicity of the 2D surface show dispersion in the surface 2D reciprocal space which results in broader bands of the surface state density N_{ss}

of the bulk electronic bands should also give rise to one surface-state level. The stronger the perturbation caused by the surface, the greater the deviation of the surface level from the bulk electronic bands. When a particular orbital is responsible for chemical bonding, e.g. the sp^3 hybrid in Si or Ge, it is strongly affected by the presence of the surface; bonds are broken, and the remaining lobes of the orbital stick out from the surface. They are called *dangling bonds*. The energy levels of such states are expected to be significantly shifted from the bulk values.

Beside these dangling-bond states there are other types of states, sometimes called *back bond* states, which are related to surface-induced modifications of the chemical bonds *between* the topmost layers. Thus the perturbation of the chemical bonds due to the presence of the surface is not restricted to the first layer of atoms. However, back bonds are generally less disturbed than dangling bonds and the corresponding surface state levels are shifted less with respect to the bulk bands.

From Fig. 6.5 it is also clear that the energetically higher-lying surface state (originating from the atomic level B) has conduction-band character, whereas the lower level which is split off from the valence band of the semiconductor is more valence-band like. The corresponding surface-state wave functions are *built up* from conduction- and valence-band wave functions which, in the absence of a surface, would have contributed to the bulk states. Therefore the charging character of the surface states also reflects that of the corresponding bulk states. A semiconductor is neutral if all conduction-band states are empty and all valence-band states are occupied by electrons. On the other hand, conduction-band states carry a negative charge if they are occupied by an electron, and valence-band states are positively charged when being unoccupied. As a consequence, surface states derived from the conduction band have the charging character

$$\text{neutral (empty)} \longleftrightarrow \text{negative (with electron)},$$

whereas surface states derived from the valence band have the character

$$\text{positive (empty)} \longleftrightarrow \text{negative (with electron)}.$$

In accordance with the definition of shallow bulk impurities one calls the first type of state (conduction-band derived) an *acceptor-type* state whereas the second is a *donor-type* state.

The simple situation depicted in Fig. 6.5 where one type of surface state derives solely from the conduction band and the other one from the valence band is only a limiting case. Most surface states are built up both from valence and conduction-band wave functions; their charging character is then determined by the relative valence and conduction-band contributions. Depending on their location within the gap (closer to valence or closer to conduction band) they are more donor or more acceptor like.

Since these intrinsic surface states have Bloch wave character for $\mathbf{k}_{/\!/}$ vectors oriented parallel to the surface (6.1), they form electronic bands in the 2D reciprocal space of the surface lattice and mostly exhibit some dispersion in $\mathbf{k}_{/\!/}$ space. Thus the sharp surface state levels (Fig. 6.5a) broaden into energetically more extended

surface state distributions (Fig. 6.5b). Due to their different charging character, more acceptor-like in the upper part and more donor-like in the lower part, there exists a neutrality energy level E_N, where the acceptor character of the states switches over into donor character. Sometimes, in particular in connection with Schottky barriers and semiconductor heterostructures (Chap. 8) this neutrality level (in the case of interface states) is called branching point energy E_B. When the surface states are occupied by electrons exactly up to E_N and empty above E_N, the surface state band is neutral, the states are not charged in total. This is a condition which will be of interest when we consider space charge regions on the surface of a semiconductor (Sect. 7.5).

A good example of the simple case depicted in Fig. 6.5 is that of partly ionic materials such as GaAs (III-V compounds). The bulk valence and conduction bands are derived essentially from As and Ga wave functions, respectively. Thus the As-derived surface states have more donor character, whereas the Ga-derived surface states are more acceptor like.

6.2.2 Extrinsic Surface States

The surface states discussed thus far are all related to the clean and well-ordered surface of a crystal with 2D translational symmetry. These states are called *intrinsic surface states*. They include the states arising due to relaxation and reconstruction. Because of the 2D translational symmetry of the surface these intrinsic surface states form electronic band structures in the 2D reciprocal space.

In addition to these states, there are other electronic states localized at a surface or interface which are related to imperfections. A missing surface atom causes a change in the bonding geometry for the surrounding atoms, thus giving rise to changes in the spectrum of electronic surface states. In particular, for crystals with partially ionic bonds, it is easily seen how a missing surface atom, i.e. ion, affects the electronic structure in the vicinity. If a negatively charged O^- ion in ZnO is missing in the topmost atomic layer, then a finite area of the surrounding surface contains more positive charge due to the surrounding Zn^+ ions than do other stoichiometric areas of the surface. This enhanced positive charge near the defect acts as a trap for electrons; in other words, the missing negative surface ion is related to a localized electronic defect state which can be occupied by an electron. Its charging character is acceptor-like. Similar behaviour is also known for III-V compounds. Missing As atoms in a GaAs surface are related to extrinsic electronic surface states which act as acceptors (Sect. 8.4).

Similar reasoning can be applied to line defects. Atoms located on the edge of a step of a non-ideal surface are in an environment different from that of an atom on an unperturbed surface. Since usually more chemical bonds are broken at an atomic step than on the flat part of an ideal surface, atoms at the edge of the step often possess more dangling-bond orbitals. The result is a new type of surface state related to step atoms. In contrast to the intrinsic states discussed before, defect-derived states do not exhibit any 2D translational symmetry parallel to the surface.

Their wave functions, of course, are localized near the defects, i.e. near the surface plane. In the particular case of a linear step, there might also be some translational symmetry along the direction of the step. Whereas intrinsic surface states are related to the existence of a perfect surface, the present *extrinsic surface* states only arise as a result of perturbations to the ideal surface.

Extrinsic surface states can also be produced by adsorbed atoms. Adsorption causes changes in the chemical bonds near the surface, thus affecting the distribution of intrinsic surface states. In addition, new electronic states are formed by the bonding and antibonding orbitals between the chemisorbed atom or molecule and the surface. Since chemisorbed atoms or molecules can form 2D lattices with translational symmetry along the surface, extrinsic electronic surface states originating from adsorbed species might form 2D band structures $E_{\mathrm{ss}}(\boldsymbol{k}_{\parallel})$ as do intrinsic surface states. The special problems related to adsorption processes on surfaces are discussed more in detail in Chap. 9.

6.3 Aspects of Photoemission Theory

6.3.1 General Description

The most important and widely used experimental technique to gain information about occupied electronic surface states is photoemission spectroscopy [6.5]. The experiment is based on the photoelectric effect [6.6]. The solid surface is irradiated by mono-energetic photons and the emitted electrons are analyzed with respect to their kinetic energy. When photons in the ultraviolet spectral range are used the technique is called UPS (UV Photoemission Spectroscopy); with X-ray radiation it is called *XPS* or *ESCA* (Electron Spectroscopy for Chemical Analysis). With synchroton radiation one can cover the whole spectral range from the near-UV to the far X-ray regime.

The use of angle-integrating electron analyzers gives integrated information about large parts of the reciprocal space, i.e. essentially one obtains the densities of occupied electronic states. In order to investigate the dispersion of electronic bands $E(\boldsymbol{k})$ and $E(\boldsymbol{k}_{\parallel})$ for bulk and surface states, respectively, a determination of the electron wave vector is necessary. Besides the kinetic energy one thus also needs to know the emission direction. This can be determined by means of an electron energy analyser with small angular aperture. The method is then known as *Angle-Resolved UV Photoemission* (ARUPS). The essential geometrical parameters in an ARUPS experiment are shown in Fig. 6.6a. The angle of incidence α of the photons (energy $\hbar\omega$), their polarization and the plane of incidence, determine the electric field direction and the vector potential $\boldsymbol{A}$ of the photoexciting electromagnetic wave with respect to the crystal lattice. The wave vector $\boldsymbol{k}^{\mathrm{ex}}$ of the emitted electrons (external of the solid) is determined by its magnitude

$$k^{\mathrm{ex}} = (2mE_{\mathrm{kin}}/\hbar^2)^{1/2} \tag{6.14}$$

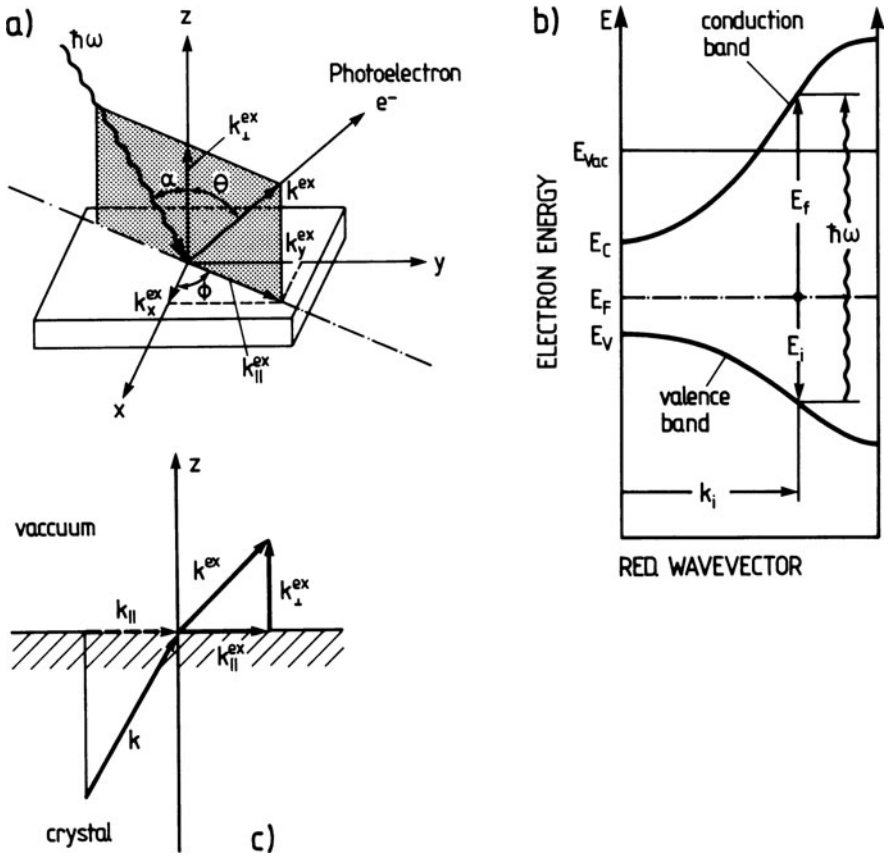

Fig. 6.6 a–c Description of a photoemission experiment. (**a**) Definition of the angles and wave vectors of the incident photon ($\hbar\omega$) and emitted electron e^-. (**b**) Representation of the photoexcitation process in the electronic band scheme $E(\boldsymbol{k})$ of a semiconductor. Only direct transitions with $\boldsymbol{k}_i \simeq \boldsymbol{k}_f$ are taken into account. The energies of the initial state (E_i) and final state (E_f) are referred to the Fermi level E_F. (**c**) Conservation of the wave vector component $\boldsymbol{k}_\parallel$, (parallel to the surface) upon transmission of the emitted electron through the surface

where E_{kin} is the kinetic energy of the detected electron, and by the emission direction described by the angles ϕ and Θ.

A rigorous theoretical approach to the photoemission process requires a full quantum-mechanical treatment of the complete coherent process in which an electron is removed from an occupied state within the solid and deposited at the detector. Theoretical approaches of this kind treat the photoeffect as a *one-step process* [6.6, 6.7]. The less accurate but simpler and more instructive approach is the so-called *three-step model* in which the photoemission process is artificially separated into three independent parts [6.8, 6.9]:

(i) Optical excitation of an electron from an initial into a final electron state within the crystal (Fig. 6.6b).
(ii) Propagation of the excited electron to the surface.
(iii) Emission of the electron from the solid into the vacuum. The electron traverses the surface (Fig. 6.6c).

In principle, these three steps are not independent of each other. For example in a more rigorous treatment the final-state wave function must be considered as consisting of the excited state function together with waves scattered from neighboring atoms. Such effects are important in the method SEXAFS (Panel VII: Chap. 7). In the three-step model the independent treatment of the above three contributions leads to a simple factorization of the corresponding probabilities in the photoemission current of the emitted electrons.

The optical excitation of an electron in the first step is simply described by the golden-rule transition probability for optical excitation:

$$\begin{aligned} W_{\mathrm{fi}} &= \frac{2\pi}{\hbar}|\langle f, \boldsymbol{k}|\mathcal{H}|\mathrm{i}, \boldsymbol{k}\rangle|^2 \delta(E_{\mathrm{f}}(\boldsymbol{k}) - E_{\mathrm{i}}(\boldsymbol{k}) - \hbar\omega) \\ &= (2\pi/\hbar) m_{\mathrm{fi}} \delta(E_{\mathrm{f}} - E_{\mathrm{i}} - \hbar\omega). \end{aligned} \tag{6.15}$$

In a first approximation direct transitions with nearly unchanged $\boldsymbol{k}$ are taken into account between the initial and final Bloch states $|\mathrm{i}, \boldsymbol{k}\rangle$ and $\langle \mathrm{f}, \boldsymbol{k}|$. The perturbation operator $\mathcal{H}$ is given by the momentum operator $\boldsymbol{p}$ and the vector potential $\boldsymbol{A}$ of the incident electromagnetic wave (dipole approximation):

$$\mathcal{H} = \frac{e}{2m}(\boldsymbol{A}\cdot\boldsymbol{p} + \boldsymbol{p}\cdot\boldsymbol{A}) \simeq \frac{e}{m}\boldsymbol{A}\cdot\boldsymbol{p} \tag{6.16}$$

with $\boldsymbol{B} = \mathrm{curl}\boldsymbol{A}$ and $\mathcal{E} = -\dot{\boldsymbol{A}}$. In (6.16) $\boldsymbol{A}$ can be assumed to commute with $\boldsymbol{p}$, since it is nearly constant in the long-wavelength limit (in UPS: $\lambda > 100$ Å). The δ-function in (6.15) describes energy conservation in the excitation of an electron from a state $E_{\mathrm{i}}(\boldsymbol{k})$ into a state $E_{\mathrm{f}}(\boldsymbol{k})$ of the electronic band structure. For the time being we consider an excitation process between two bulk bands $E_{\mathrm{i}}(\boldsymbol{k})$ and $E_{\mathrm{f}}(\boldsymbol{k})$; simplifications that arise for excitations between surface-state bands are explained later.

Outside the solid on the vacuum side one can only detect electrons whose energy E is above the vacuum energy E_{vac} (Fig. 6.6b) and whose $\boldsymbol{k}$ vector in the final state is directed outwards from the surface, i.e. $k_\perp > 0$.

The internal electron current density directed towards the surface with an energy E and a wave vector around $\boldsymbol{k}$ is therefore ($k_\perp > 0$)

$$I^{\mathrm{int}}(E, \hbar\omega, \boldsymbol{k}) \propto \sum_{\mathrm{fi}} m_{\mathrm{fi}} \mathrm{f}(E_{\mathrm{i}}) \delta(E_{\mathrm{f}}(\boldsymbol{k}) - E_{\mathrm{i}}(\boldsymbol{k}) - \hbar\omega) \delta(E - E_{\mathrm{f}}(\boldsymbol{k})). \tag{6.17}$$

For detection at energy E (which involves adjusting the energy window of the electron analyser), the energy of the final state $E_f(\boldsymbol{k})$ has to equal E. The function $f(E_i)$ is the Fermi distribution function. It ensures that the initial state with E_i is occupied.

The second step in the three-step model is the propagation of the electrons described by (6.17) to the surface. A large number of electrons undergo inelastic scattering processes; they lose part of their energy E_f (or E) by electron-plasmon or electron-phonon scattering. Such electrons contribute to the continuous background in the photoemission spectrum which is called the *true secondary background*; they have lost the information about their initial electronic level E_i (Fig. 6.6). The probability that an electron will reach the surface without inelastic scattering is given phenomenologically by the mean-free path λ. In general, λ depends on the energy E, the electron wave vector $\boldsymbol{k}$ and on the particular crystallographic direction. The propagation to the surface is thus described in a simplifying manner by the *transport probability* $D(E, \boldsymbol{k})$ which is proportional to the mean free

$$D(E, \boldsymbol{k}) \propto \lambda(E, \boldsymbol{k}). \tag{6.18}$$

It is this second step of propagation to the surface which makes photoemission a surface sensitive technique. The value of λ is typically between 5 and 20 Å (Fig. 4.1), thus limiting the information depth to this spatial region.

The third step, transmission of the photoexcited electron through the surface can be considered as the scattering of a Bloch electron wave from the surface-atom potential with translational symmetry parallel, but not normal to the surface. One arrives at the same conclusions when the transmission through the surface is thoroughly treated by matching the internal Bloch wave functions to free-electron wave functions (LEED problem, Sect. 4.4) outside on the vacuum side. In any case, because of the 2D translational symmetry, the transmission of the electron through the surface into the vacuum requires conservation of its wave-vector component parallel to the surface (Fig. 6.6c):

$$\boldsymbol{k}_{\parallel}^{\mathrm{ex}} = \boldsymbol{k}_{\parallel} + \boldsymbol{G}_{\parallel}; \tag{6.19}$$

where $\boldsymbol{k}$ is the wave vector of the electron inside the crystal. Its component normal to the surface $\boldsymbol{k}_{\perp}$ is not conserved during transmission through the surface. For the external electron on the vacuum side, the $k_{\parallel}^{\mathrm{ex}}$ value is determined by the energy conservation requirement

$$E_{\mathrm{kin}} = \frac{\hbar^2 k^{\mathrm{ex}^2}}{2m} = \frac{\hbar^2}{2m}(k_{\perp}^{\mathrm{ex}^2} + k_{\parallel}^{\mathrm{ex}^2}) = E_f - E_{\mathrm{vac}}. \tag{6.20}$$

With $\phi = E_{\mathrm{vac}} - E_F$ as the work function and E_B as the (positive) binding energy referred to the Fermi level E_F (Fig. 6.6b) one also has

$$\hbar\omega = E_f - E_i = E_{\mathrm{kin}} + \phi + E_B. \tag{6.21}$$

The wave-vector component parallel to the surface outside the crystal [from (6.20, 6.21)], which is determined from known experimental parameters,

$$k_{\parallel}^{\mathrm{ex}} = \sqrt{\frac{2m}{\hbar^2}}\sqrt{\hbar\omega - E_{\mathrm{B}} - \phi}\,\sin\Theta = \sqrt{\frac{2m}{\hbar^2}E_{\mathrm{kin}}}\,\sin\Theta \tag{6.22}$$

therefore directly yields the internal wave-vector component $k_{\parallel}$ according to (6.19).

On the other hand, due to the inner microscopic surface potential V_0, the wave-vector component $k_{\perp}$ of the electron inside the crystal is changed upon transmission through the surface. The outside component is determined by energy conservation according to (6.20) as

$$k_{\perp}^{\mathrm{ex}} = \sqrt{\frac{2m}{\hbar^2}E_{\mathrm{kin}} - (\boldsymbol{k}_{\parallel} + \boldsymbol{G}_{\parallel})^2} = \sqrt{\frac{2m}{\hbar^2}E_{\mathrm{kin}}}\,\cos\Theta. \tag{6.23}$$

However, without a detailed knowledge of the electronic band structure for energies above E_{vac} and of the inner microscopic potential V_0 (usually not exactly known) information about the inner wave-vector component $k_{\perp}$ cannot be obtained.

According to (6.19) the third step, transmission through the surface, can be described formally by the transmission rate

$$T(E,\boldsymbol{k})\delta(\boldsymbol{k}_{\parallel} + \boldsymbol{G}_{\parallel} - \boldsymbol{k}_{\parallel}^{\mathrm{ex}}). \tag{6.24}$$

In the simplest and rather naive approach one might assume that $T(E,\boldsymbol{k})$ is a constant $R \leq 1$ with

$$T(E,\boldsymbol{k}) = \begin{cases} 0 \text{ for } k_{\perp}^{\mathrm{ex}^2} = \frac{2m}{\hbar^2}(E_{\mathrm{f}} - E_{\mathrm{vac}}) - (\boldsymbol{k}_{\parallel} + \boldsymbol{G}_{\parallel})^2 < 0, \\ R \text{ for } k_{\perp}^{\mathrm{ex}^2} = \frac{2m}{\hbar^2}(E_{\mathrm{f}} - E_{\mathrm{vac}}) - (\boldsymbol{k}_{\parallel} + \boldsymbol{G}_{\parallel})^2 > 0. \end{cases} \tag{6.25}$$

This form (6.25) of $T(E,\boldsymbol{k})$ takes into account that only electrons with the positive wave-vector component $k_{\perp}^{\mathrm{ex}}$ can be observed in the photoemission experiment; all others are unable to reach the vacuum side of the crystal surface and are internally reflected since their kinetic energy is not sufficient to surmount the surface barrier.

Taking together (6.15, 6.17, 6.18, 6.24, 6.25) one arrives at the following formula for the observable (external) emission current in the three-step model:

$$\begin{aligned} I^{\mathrm{ex}}(E,\hbar\omega,\boldsymbol{k}_{\parallel}^{\mathrm{ex}}) &= I^{\mathrm{int}}(E,\hbar\omega,\boldsymbol{k})D(E,\boldsymbol{k})T(E,\boldsymbol{k})\delta(\boldsymbol{k}_{\parallel} + \boldsymbol{G}_{\parallel} - \boldsymbol{k}_{\parallel}^{\mathrm{ex}}) \\ &\propto \sum_{\mathrm{f,i}} m_{\mathrm{fi}}\mathrm{f}(E_{\mathrm{i}}(\boldsymbol{k}))\delta(E_{\mathrm{f}}(\boldsymbol{k}) - E_{\mathrm{i}}(\boldsymbol{k}) - \hbar\omega)\delta(E - E_{\mathrm{f}}(\boldsymbol{k})) \\ &\quad \times \delta(\boldsymbol{k}_{\parallel} + \boldsymbol{G}_{\parallel} - \boldsymbol{k}_{\parallel}^{\mathrm{ex}})D(E,\boldsymbol{k})T(E,\boldsymbol{k}_{\parallel}). \end{aligned} \tag{6.26}$$

The following discussion reveals what kind of information can be extracted from a photoemission spectrum.

6.3.2 Angle-Integrated Photoemission

If in the photoemission experiment one uses an electron energy analyzer that accepts (in the ideal case) electrons within the whole half-space above the sample surface, then the total photocurrent contains contributions with every possible $\boldsymbol{k}_\parallel$. Such an angle integrated measurement can be achieved to a good approximation by using a (LEED) retarding field analyser (Panel VIII: Chap. 4). The total measured photocurrent is obtained by integrating (6.26) over $\boldsymbol{k}_\parallel^{\mathrm{ex}}$. With the restrictions (6.22, 6.23), i.e. conservation of $\boldsymbol{k}_\parallel$ and determination of $k_\perp$ by energy conservation, the integration over $\boldsymbol{k}_\parallel^{\mathrm{ex}}$ can be transformed into an integration over the whole $\boldsymbol{k}$ space, i.e.,

$$\tilde{I}^{\mathrm{ex}}(E, \hbar\omega) \propto \int_{\text{half sphere}} I^{\mathrm{ex}}(E, \hbar\omega, \boldsymbol{k}_\parallel^{\mathrm{ex}}) \mathrm{d}\boldsymbol{k}^{\mathrm{ex}}. \tag{6.27a}$$

The integration cancels the $\delta(\boldsymbol{k}_\parallel + \boldsymbol{G}_\parallel - \boldsymbol{k}_\parallel^{\mathrm{ex}})$ function. Assuming furthermore that the matrix elements m_{fi} are slowly varying functions in $\boldsymbol{k}$ space, one arrives at an expression for the total external photoemission current:

$$\tilde{I}^{\mathrm{ex}}(E, \hbar\omega) \propto \sum_{\mathrm{f,i}} m_{\mathrm{fi}} \int \mathrm{d}\boldsymbol{k} \mathrm{f}(E_{\mathrm{i}}(k)) \delta(E_{\mathrm{f}}(\boldsymbol{k}) - E_{\mathrm{i}}(\boldsymbol{k}) - \hbar\omega) \delta(E - E_{\mathrm{f}}(\boldsymbol{k})). \tag{6.27b}$$

This expression includes all possible ways in which an electron can be excited from the occupied band $E_{\mathrm{i}}(\boldsymbol{k})$ to the band $E_{\mathrm{f}}(\boldsymbol{k})$ with the restriction of energy and wavevector conservation. The $\delta(E - E_{\mathrm{f}}(\boldsymbol{k}))$ selects only those final states whose energy E_{f} coincides with the detection energy E. The current is therefore proportional to the joint density of states for which the final states have the energy E. The information obtained is similar to that yielded by an optical absorption experiment, but the final-state distribution enters via $\delta(E - E_{\mathrm{f}}(\boldsymbol{k}))$.

When lower photon energies are used, i.e. UPS rather than XPS, the final states, that can be reached (in UPS), may have a considerably structured density of states giving rise to strong changes of the photoemission current $\tilde{I}^{\mathrm{ex}}$ (6.27) with varying photon energy. In XPS, on the other hand, the photon energies are quite high and the final states are distributed quasi-continuously. The photocurrent becomes relatively insensitive against variations in photon energy. The structure obtained is then determined largely by the distribution of the initial states $E_{\mathrm{i}}(\boldsymbol{k})$. Angle-integrated (but also non-integrated) UPS and XPS are particularly useful as a finger-printing technique to identify an adsorbed species by the characteristic emission lines from its molecular orbitals (Fig. 6.7) [6.10].

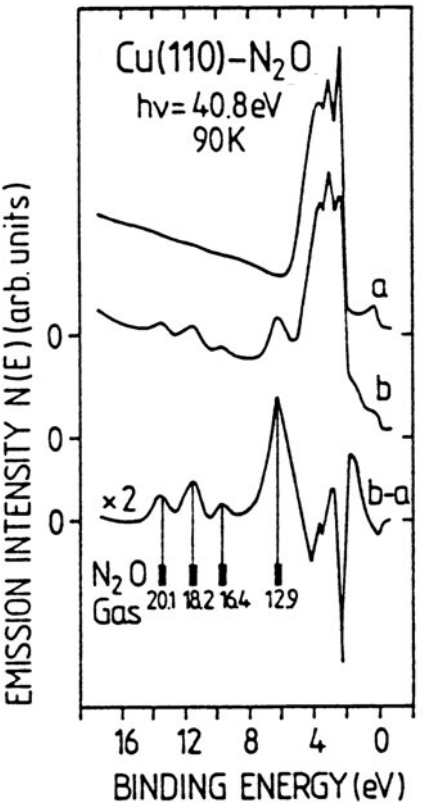

Fig. 6.7 He II UPS spectra of a clean Cu(110) surface at 90 K (**a**), and after a 1 L exposure to N_2O (**b**). Marked under the difference curve (**b–a**), enlarged by a factor of 2, are the vertical ionization energies of gaseous N_2O (referred to vacuum level) [6.10]

6.3.3 Bulk- and Surface-State Emission

According to (6.19, 6.22) the externally determined wave-vector component $\boldsymbol{k}_{\parallel}^{\mathrm{ex}}$ directly provides the internal component $\boldsymbol{k}_{\parallel}$. For 2D band structures of surface-state bands or electronic states of regularly adsorbed molecules this is sufficient. All information about the wave vectors of the states is given. The same is true for quasi 2D crystals composed of lamellar structures (graphite, $TaSe_2$, etc.). When using ARUPS for the determination of 3D band structures of bulk electronic states one is faced with the problem of determining the $\boldsymbol{k}_{\perp}$ component inside the solid. Since $k_{\perp}$ is not conserved, the value measured outside $k_{\perp}^{\mathrm{ex}}$ (6.23) does not yield this information. Several approaches are used to overcome this problem. One can measure the photoemission spectra for various photon energies under normal emission ($\Theta = 0$ in Fig. 6.5a) thus having vanishing wave-vector components $\boldsymbol{k}_{\parallel}$, $\boldsymbol{k}_{\parallel}^{\mathrm{ex}}$ parallel to the surface. The wave vector components $k_{\perp}^{\mathrm{ex}}$ and $k_{\perp}$ outside and inside the crystal are related via energy conservation and the internal potential V_0. As a simple approximation one sometimes assumes *free electron parabolae* for the final states

$$E_{\mathrm{f}}(k_{\perp}) \simeq \hbar^2 \frac{k_{\perp}^2}{2m^*}. \tag{6.28}$$

The kinetic energy of the electron in the vacuum is given by

$$E_{\mathrm{kin}} = \hbar^2 \frac{k_{\perp}^{\mathrm{ex}^2}}{2m} = \frac{\hbar^2 k_{\perp}^2}{2m^*} + V_0. \tag{6.29}$$

A further assumption about the inner potential, e.g. the zero of a muffin-tin potential, then allows an unequivocal determination of $E_{\mathrm{i}}(k_{\perp})$ from the measured outside quantities E_{kin} and $k_{\perp}^{\mathrm{ex}} = k^{\mathrm{ex}}$. If band-structure calculations are available, one can also use the theoretical final-state bands $E_{\mathrm{f}}(\boldsymbol{k})$ instead of (6.28) to calculate the internal $k_{\perp}$ value from the measured value $k_{\perp}^{\mathrm{ex}}$. In a trial-and-error procedure one can thus compare a progressively improved theoretical band structure, including both $E_{\mathrm{i}}(\boldsymbol{k})$ and $E_{\mathrm{f}}(\boldsymbol{k})$ with the measured data.

There is another direct experimental approach to the problem of $k_{\perp}$ determination which is shown for the example of clean Au surfaces in Fig. 6.8 [6.11]. In order to determine the electronic band structure $E(\boldsymbol{k})$ along a certain symmetry line, in this case along ΓL (Fig. 6.8b), angle-resolved photoemission measurements normal to the surface of Au(111) are performed. Because of $\boldsymbol{k}_{\parallel} (\simeq 0)$ conservation only states

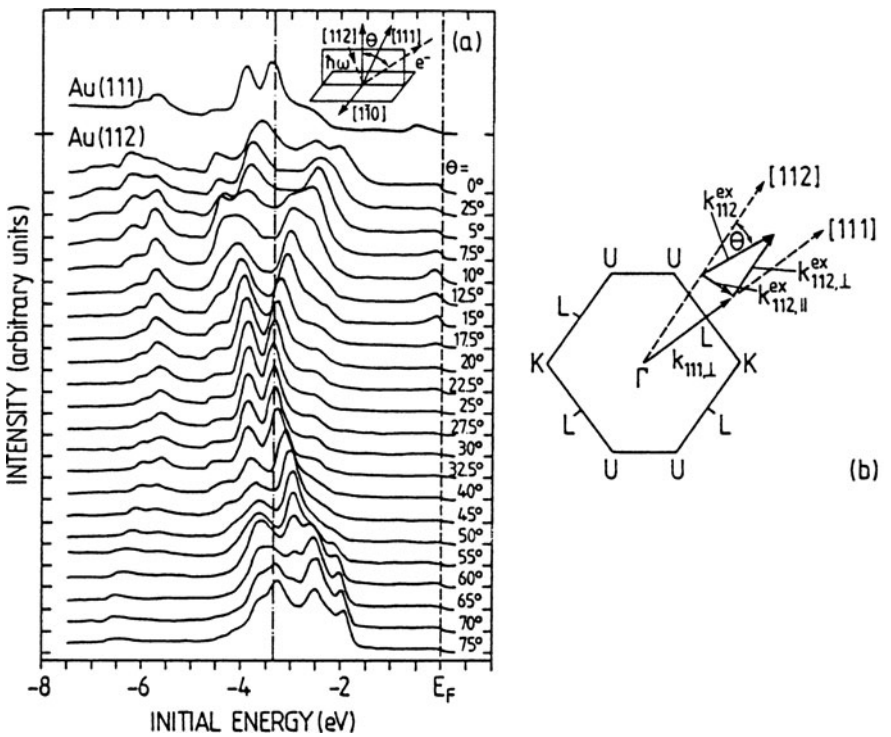

Fig. 6.8 (**a**) Normal ARUPS photoemission spectra from Au(111) and a family of spectra from Au(112) obtained at different polar emission angles Θ (explanation in inset). The photon energy $\hbar\omega$ is 16.85 eV. (**b**) Cut through the Brillouin zone with the emission directions of (**a**) indicated. Projection of the wave vector component $\boldsymbol{k}_{112,\parallel}$ onto the ΓL direction yields the wave vector $\boldsymbol{k}_{111,\perp}$ i.e. the location of the final state in $\boldsymbol{k}$-space [6.11]

described by wave vectors normal to the considered (111) surface, i.e. in the ΓL direction contribute to the normal photoemission from Au(111). The direction in $\boldsymbol{k}$ space is thus known for the measured spectrum on Au(111) in Fig. 6.8a, but not the actual length of the internal wave vector. If ARUPS measurements from another surface of the crystal, e.g. the Au(112) surface, are now performed (Fig. 6.8a) under different polar angles Θ with respect to [112], one might be able to identify the same emission bands in one of those spectra as for the normal measurement along [111]. In Fig. 6.8a the spectrum with $\Theta = 25°$ best resembles the upper spectrum on Au(111). From the measured binding energies E_B, the work function ϕ on Au(112) and the angle Θ the corresponding wave vectors $\boldsymbol{k}^{\mathrm{ex}}_{112}$ are calculated, and according to (6.22) also the parallel component $\boldsymbol{k}^{\mathrm{ex}}_{112,\parallel}$ which is identical to the internal wave vector $\boldsymbol{k}_{112,\parallel}$. After projecting $\boldsymbol{k}_{112,\parallel}$ on the ΓL direction (Fig. 6.8b) one obtains the location of the contributing final states in $\boldsymbol{k}$ space, i.e., the wave vector $\boldsymbol{k}_{111,\perp}$ (1.94 ± 0.11 Å^{-1} in Fig. 6.8b).

Although the investigation of a 2D band structure is straightforward as far as the determination of $\boldsymbol{k}_\parallel$ is concerned, there is a problem in distinguishing between bulk and surface emission bands in the photoemission spectrum. Four criteria can help one to decide whether a particular band arises from surface states, i.e. is due to a 2D band structure $E_\mathrm{i}(\boldsymbol{k}_\parallel)$ localized at the very surface

(i) Since no definite $k_\perp$ exists for surface-state emission, (6.22) must be fulfilled for every possible choice of photon energy, i.e. one and the same dispersion $E_\mathrm{i}(\boldsymbol{k}_\parallel)$ must be obtained by using different photon energies.
(ii) For measurements at normal emission the parallel components $k^{\mathrm{ex}}_\parallel$ and $k_\parallel$ vanish. For emission from a surface-state band $E_\mathrm{ss}(\boldsymbol{k}_\parallel)$ the band structure then contributes at the Γ point ($k_\parallel = 0$) only, independent of the photon energy used. A surface-emission band thus occurs at the same energy in the spectrum for different photon energies. In contrast, a bulkemission band is expected to vary in energetic position with changing photon energy.
(iii) An emission band from real surface states must fall into a bulk-band gap. Thus, if a plot of the measured $E(\boldsymbol{k}_\parallel)$ dependence is not degenerate with the projected bulk-band structure (Fig. 6.4), this suggests surface-state emission.
(iv) In contrast to surface states, bulk states are not affected by a surface treatment. If an emission band of the clean surface vanishes after gas adsorption, its origin is likely to be surface states. But care must be taken in applying this rule, since adsorption might also change the transmission conditions for electrons through the surface (due, e.g., to space charge layers.).

6.3.4 Symmetry of Initial States and Selection Rules

According to (6.15, 6.16) the photocurrent in ARUPS is determined by matrix elements of the form

$$m_\mathrm{fi} = \langle \mathrm{f}, \boldsymbol{k} | \frac{e}{m} \boldsymbol{A} \cdot \boldsymbol{p} | \mathrm{i}, \boldsymbol{k} \rangle, \tag{6.30}$$

where $\boldsymbol{A}$ is the vector potential of the incoming UV light or X-rays, and $\boldsymbol{p}$ is the momentum operator ($\boldsymbol{p} = \hbar\nabla/\mathrm{i}$). By considering special experimental geometries and the symmetry of the electronic states involved, we can derive interesting selection rules for the observability of particular initial states $|\mathrm{i}, \boldsymbol{k}\rangle$. We assume that the surface has a mirror plane (Fig. 6.9), and that both the direction of incidence of the exciting light and the detection direction for the emitted electrons are within that mirror plane (yz).

The initial electronic states $|\mathrm{i}, \boldsymbol{k}\rangle$ can be classified as being even or odd with respect to reflection in the mirror plane, i.e. they retain or change their sign upon reflection. The final-state wave function must always be even, otherwise a detector located in the mirror plane would see a node of the emitted electron. We now consider two possible polarizations of the incoming exciting light. If the vector potential $\boldsymbol{A}_1$ is parallel to the mirror plane (yz) (Fig. 6.9) the momentum operator contains only components $\partial/\partial y$ and $\partial/\partial z$ that are even with respect to reflection in the mirror plane. If $\boldsymbol{A}_2$ is oriented normal to the mirror plane, only $\partial/\partial x$ (odd) occurs in the perturbation operator in (6.30). In order to detect a photoemission signal for both polarizations one requires:

$$\text{for } \boldsymbol{A}_1 \| (xy): \quad \langle \mathrm{f}, \boldsymbol{k}| \frac{\partial}{\partial y} |\mathrm{i}, \boldsymbol{k}\rangle \neq 0, \ \langle \mathrm{f}, \boldsymbol{k}| \frac{\partial}{\partial z} |\mathrm{i}, \boldsymbol{k}\rangle \neq 0, \tag{6.31a}$$

with $\langle \mathrm{f}, \boldsymbol{k}|$, $\partial/\partial y$, $\partial/\partial z$ and $|\mathrm{i}, \boldsymbol{k}\rangle$ even;

$$\text{for } \boldsymbol{A}_2 \perp (yz): \quad \langle \mathrm{f}, \boldsymbol{k}| \frac{\partial}{\partial x} |\mathrm{i}, \boldsymbol{k}\rangle \neq 0. \tag{6.31b}$$

with $\langle \mathrm{f}, \boldsymbol{k}|$ even and $\partial/\partial x$, $|\mathrm{i}, \boldsymbol{k}\rangle$ odd.

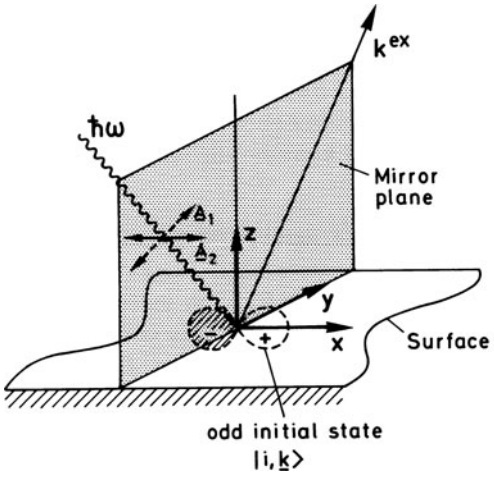

Fig. 6.9 Symmetry selection rule in a photoemission experiment. The direction of the incident light ($\hbar\omega$) and the trajectory of the emitted electron (wave vector $\boldsymbol{k}^{\mathrm{ex}}$) lie in a mirror plane of the crystal surface. The electron is emitted from an initial state $|\mathrm{i}, \boldsymbol{k}\rangle$ that is of odd parity with respect to the mirror plane. Since the final state must be even with respect to the mirror plane, only a light polarization $\boldsymbol{A}_2$ (vector potential of the light wave) normal to the yz plane gives rise to a measurable emission from this initial state $|\mathrm{i}, \boldsymbol{k}\rangle$

The fact that the final states $\langle \mathrm{f}, \boldsymbol{k}|$ are always even, implies, for the geometry $\boldsymbol{A}_1 \parallel (yz)$, that the initial state must be even with respect to reflection on the mirror plane (yz). An s-type wave function as initial state would lead to an emission signal, whereas a p-type orbital oriented along the x-axis as in Fig. 6.9 would not be detected in this experimental geometry. On the other hand, an odd initial state can be observed, according to (6.31b), when the light is polarized with $\boldsymbol{A}_2$ normal to the mirror plane. Thus by measuring the photocurrent in a surface mirror plane for light polarized in and perpendicular to this plane, one can determine an important property of the initial state, namely its reflection symmetry. However, when spin-orbit coupling is important, odd and even states are mixed and the polarization selection rule is no longer strictly valid. An appropriate choice of the experimental geometry in ARUPS can give important information about the symmetry character (s-, p- or d-like) of electronic surface-state bands and also about molecular orbitals of adsorbates.

6.3.5 Many-Body Aspects

So far, our discussion of the photoemission experiment has been based on the one-electron states of a system of non-interacting electrons. Such a system, be it an atom, a molecule or a crystal consisting of N electrons, is described by a simple many-electron wave function, i.e.,

$$\Psi = \phi_1(\boldsymbol{r}_1)\phi_2(\boldsymbol{r}_2).\ldots.\phi_N(\boldsymbol{r}_\mathrm{N}), \tag{6.32}$$

which is the product of the single one-electron functions $\phi_\mathrm{i}(\boldsymbol{r}_\mathrm{i})$. Correspondingly the total energy E_N of such a non-interacting system is the sum of one-electron energies ϵ_i:

$$E_\mathrm{N} = \epsilon_1 + \epsilon_2 + \epsilon_3 + \ldots.. + \epsilon_N. \tag{6.33}$$

In a photoemission experiment in which an electron is emitted from the energy level ϵ_ν the measured binding energy E_B in (6.21) is the difference between the initial total energy E_N of the N-electron system and E_{N-1}, that of the $(N-1)$ electron system:

$$E_\mathrm{B} = E_N - E_{N-1} = \epsilon_\nu. \tag{6.34}$$

This binding energy directly yields the energy of the νth electron in its one-electron state. In reality this picture is too simple since the electron–electron interaction cannot be neglected. The real many-body wave function cannot be written as a product (6.32) and the total energy E'_N of the N-electron system is not merely the sum of one-electron energies as in (6.33). In a HartreeFock treatment one can, of course, define single-electron energy levels ϵ'_ν. These, however, are dependent on the presence or absence of all the other $N-1$ electrons. The removal of an electron from such an interacting N-electron system causes the remaining $(N-1)$ electrons to

rearrange in the new potential in response to the creation of the hole. The $(N-1)$ electron system "relaxes" into a new many-body state of minimal energy E'_{N-1}. The energy difference, termed the *relaxation energy* E_R, is passed on to the photoelectron, which then appears at higher kinetic energy, i.e. the measured binding energy E_B is not just a one-electron energy ϵ'_ν (in the HartreeFock sense) but includes a contribution due to this relaxation effect (or shielding of the hole):

$$E_B = \epsilon'_\nu - E_R. \tag{6.35}$$

The accuracy to which a Hartree-Fock single electron eigenvalue ϵ'_ν approximates the measured binding energy (or ionization potential) depends on how strongly the eigenvalue is influenced by the occupation with other electrons. If this effect can be neglected, the so-called *Koopmans theorem* holds, i.e. the binding energy is essentially the one-electron Hartree-Fock energy of the state.

The particular sensitivity of X-ray photoemission from core levels to the chemical environment of an atom (e.g., C bound to three H or to a C and two O atoms in Fig. 6.10) has given XPS its alternative name ESCA (Electron Spectroscopy for Chemical Analysis). The electron configuration of the neighboring chemical bonds determines the local electrostatic potential for the core levels and thereby influences the relaxation energy E_R and the shielding of the photoexcited core hole. As seen from Fig. 6.10, XPS or ESCA can be used as a fingerprinting technique to locate certain atoms in a molecule by their *core-level shifts*. The same is true for adsorbed atoms on a substrate.

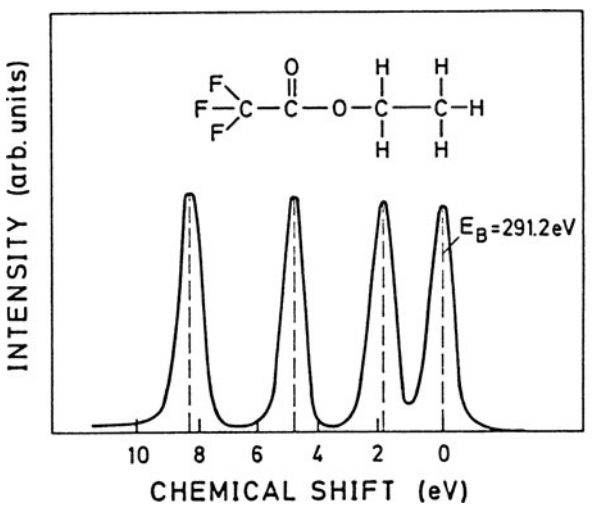

Fig. 6.10 X-ray photoemission spectrum (ESCA) of the carbon core level with a binding energy of about 291 eV, obtained from the molecule $C_2H_5CO_2CF_3$. According to the different chemical surroundings of the carbon atoms in the molecule, slightly different energies are found for the core level (chemical shift). The order of the lines corresponds to the order of the C atoms in the molecule above [6.12]

So far we have assumed that the relaxation of the N-electron system leads to the ground state of the new $(N-1)$-electron system. The relaxation might, however, be *incomplete*, thus yielding an excited state of the $(N-1)$-electron system. Depending on the strength of the coupling between the surrounding electrons and the photoexcited hole (be it in the valence or core-level energy regime, UPS or XPS), collective excitations such as phonons, plasmons or interband transitions might be excited during the relaxation process. The photoemitted electron then receives only a part of the relaxation energy E_R, (6.35), the remainder having been used to excite a plasmon, interband transition, etc. The photoelectron is detected in a so-called *satellite peak* at an energy different from E_B (6.35). These satellite peaks can complicate the theoretical analysis of UPS and XPS spectra considerably if they are not identified as satellites.

The relaxation sometimes also called *relaxation/polarization effect* discussed so far concerns a single multi-electron system such as an atom, a molecule or a solid. The corresponding shifts E_R are thus more accurately termed intramolecular relaxation shifts. When we consider an atom or a molecule adsorbed on a solid surface, photo-excitation of an electron from such an adsorbate creates a valence or core hole (in UPS or XPS) in an environment different from that in the free atom or molecule. The relaxation process from the N electron ground state into the $(N-1)$-electron state also involves electrons in the adsorbate's chemical bond and possibly those in the substrate surface. In addition, the photoemitted electron leaving the adsorbate-surface complex is accompanied by an image charge (also a manybody shielding effect) within the substrate (Fig. 6.11). The attractive interaction between the photoelectron and its image further contributes to the adsorption-induced change of E_R. This change of E_R due to adsorption is called "extramolecular" Relaxation/Polarization (R/P) shift. Experimentally this extramolecular R/P shift is evaluated by comparing photoemission spectra of an adsorbed species with

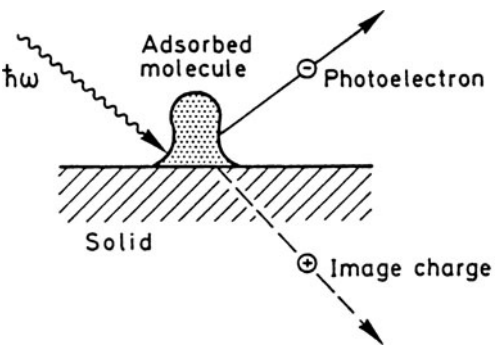

Fig. 6.11 Schematic explanation of the extramolecular relaxation/polarization of a photoelectron emitted from an adsorbed molecule. The solid substrate participates in the relaxation of the many electron system after emission of an electron from the adsorbed molecule and therefore produces an additional shift of the emission line. Furthermore, the photoelectron is associated with an image charge within the substrate whose Coulomb interaction also changes its kinetic energy

those of its gas phase counterpart (Fig. 6.7). If one compares the measured binding energies referred to the same vacuum level, the gas-phase ionization potentials always exceed the binding energies of the adsorbed species by 1 to 3 eV (Fig. 6.7).

As well as these so-called *final state effects* there are also "initial state" effects which might cause shifts of particular valence state emission lines with respect to their gas phase lines in UPS. These shifts arise from bonding interactions between the substrate and special adsorbate orbitals (chemical bonding shifts).

6.4 Some Surface-State Band Structures for Metals

Historically, electron surface states on metals were detected much later than on semiconductor surfaces. The reason was that ARUPS was necessary for determining the $\boldsymbol{k}$ vector of a particular state to see if its energy falls into a bulk-state gap. Without angular resolution a surface state can hardly be seen on a metal because of the high background of the integrated bulk-state density. In semiconductors, where an absolute forbidden gap is present, surface states located in the energy gap have a strong influence on the electronic properties of the surface (Chap. 7) and are therefore easily detected experimentally.

6.4.1 s- and p-like Surface States

Simple metals such as Na, Mg and Al have an electronic band structure that strongly resembles that of the simple model of a free electron gas. The bulk bands derived from atomic s- and p-states have a nearly parabolic shape. At the Brillouin-zone boundaries and near other crossings of the "free electron" parabolae, gaps occur which also exhibit parabolic shape. Thus, in these cases one can apply surface-state theory in its simplest form based on the "nearly free electron" model (or slightly modified versions). Experimental band structures have been obtained by means of ARUPS. As an example, Fig. 6.12 depicts photoemission spectra for Al(100) under normal emission ($\Theta_e = 0$) measured with various photon energies $\hbar\omega$. Figure 6.13 exhibits the results of measurements made at various angles of detection, i.e. with varying $\boldsymbol{k}_\parallel$ [6.13]. The sharp emission band A in Fig. 6.12, which is essentially independent of photon energy but shifts with $\boldsymbol{k}_\parallel$ (Fig. 6.13) is due to a surface-state emission. In Fig. 6.14 its energetic position is plotted as a function of the $\boldsymbol{k}_\parallel$ vector calculated according to (6.22). The comparison with the bulk-band structure of Al along $\overline{\Gamma M}$ and $\overline{\Gamma X}$ reveals that the photoemission data definitely fall into a gap of the nearly free (parabolic) electron states along these symmetry lines. This is a clear indication of a surface state band. Its parabolic shape, similar to that of the bulk states, shows that it originates from free electron-like states. This band appears to be split off from the corresponding bulk band. The same bulk

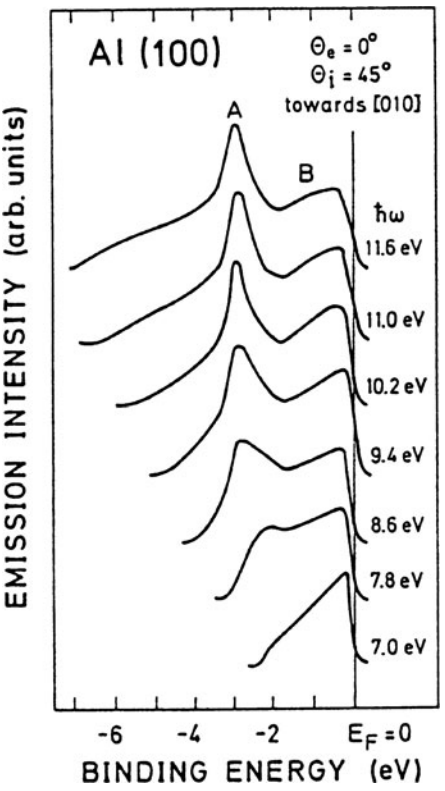

Fig. 6.12 Experimental spectra of photoelectrons emitted normal to the Al(100) surface for photon energies between 7 and 11.6 eV (direction of incidence 45° to the [011] direction) [6.13]

bands, when projected onto the (101) surface, exhibit a further parabolic gap in which another split-off surface-state band (dark data points) is found (Fig. 6.15). The $\boldsymbol{k}_\parallel$ direction on the Al(101) surface is along $\overline{\Gamma X}$ of the surface Brillouin zone.

Similar *sp*-state-derived surface-state bands are well-known for the transition metals Au [6.16] and Cu [6.17]. In Cu the *d* levels are occupied and lie about 2 eV below the Fermi level. The bulk states between these and the Fermi level are all *sp*-derived. Figure 6.16 shows some photoemission spectra measured at normal emission from a Cu(111) surface with several photon energies [6.17]. The peak *S* visible at an amplification of 10 is definitely due to surface states. At normal emission ($\boldsymbol{k}_\parallel = \boldsymbol{0}$) it does not change its energetic position when the photon energy is varied. The dispersion $E(\boldsymbol{k}_\parallel)$ can easily be measured by changing the detection angle (Fig. 6.17). Figure 6.18 displays the dispersion of this surface-state band measured with two different photon energies (cf. the argument in favor of surface-state emission in Sect. 6.3.2). The band is parabolic, as expected for *sp*-derived states. The points lie in a gap of the projected bulk sp states just below the Fermi level. A similar parabolic band of *sp*-derived surface states has also been detected on the Cu(110) surface near the $\overline{Y}$ point of the 2D Brillouin zone (Fig. 6.19).

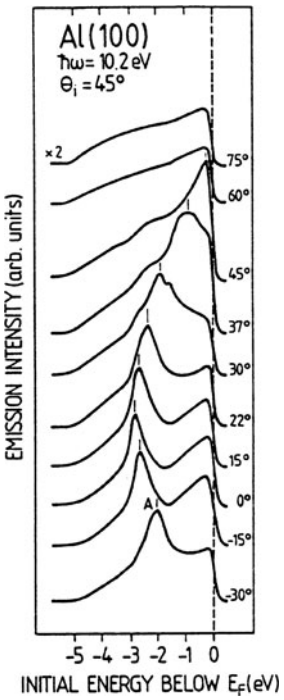

Fig. 6.13 Photoemission spectra from the Al(100) surface with different polar angles in the $(01\bar{1})$ plane; photon energy $\hbar\omega = 10.2\,\mathrm{eV}$, (direction of incidence 45° to the [011] direction) [6.13]

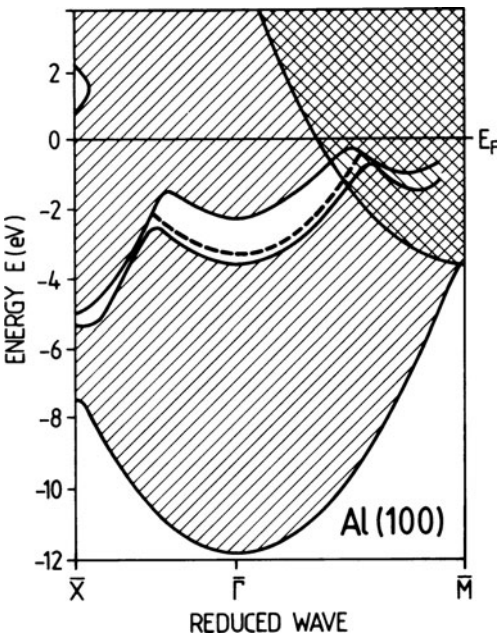

Fig. 6.14 Measured surface state dispersion (broken curve [6.13]) and projected bulk bands for Al(100) (shaded area [6.15]) [6.14]

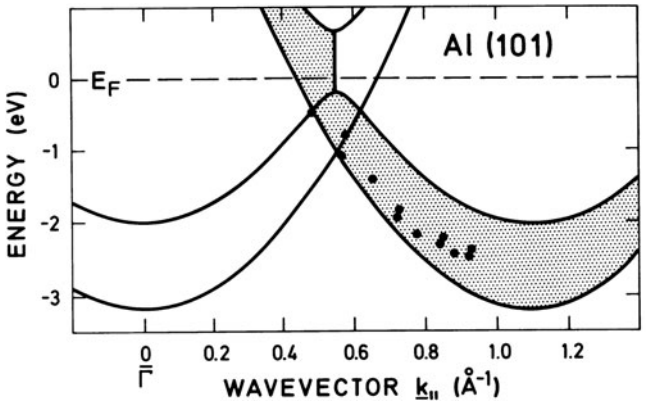

Fig. 6.15 Dispersion of *sp*-derived surface state band on the Al(101) surface as obtained from ARUPS. The data points fall into a gap (shaded) of the projected bulk-band structure [6.13]

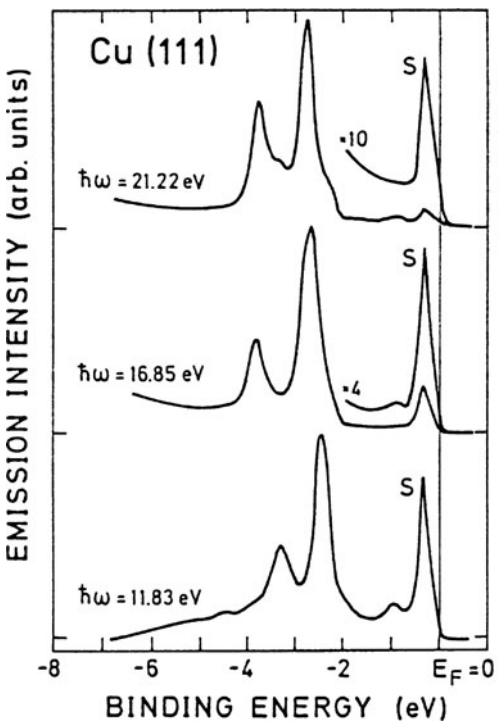

Fig. 6.16 Normal emission ARUPS data obtained from the Cu(111) surface with different photon energies. The sharp peak *S* is due to a surface-state band [6.17]

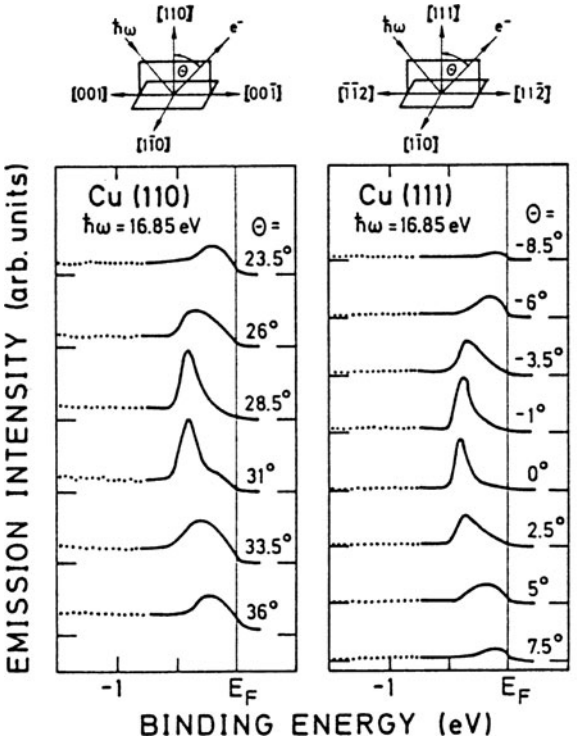

Fig. 6.17 Angle-resolved UV-photoemission spectra of surface-state bands on the Cu(110) and Cu(111) surface. The peak shifts as a function of detection angle Θ indicate a significant dispersion [6.17]

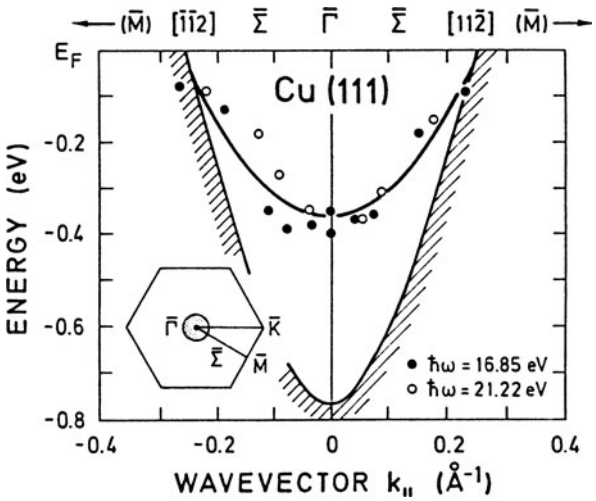

Fig. 6.18 Dispersion of the *sp*-derived surface state band on Cu(111) according to the ARUPS data of Fig. 6.17. Data points from measurements with two different photon energies $\hbar\omega$ are plotted in the gap of the projected bulk bands (shaded). The inset gives the location in reciprocal space [6.17]

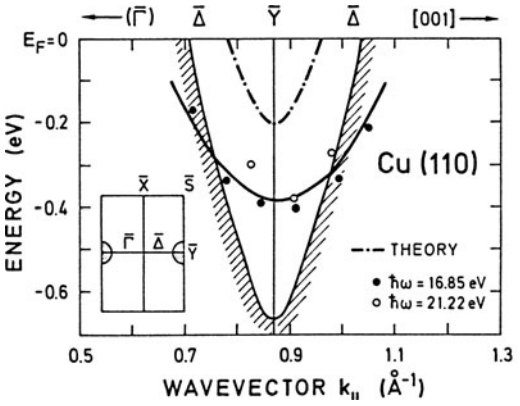

Fig. 6.19 Dispersion of the *sp*-derived surface state band on Cu(110) according to the ARUPS data in Fig. 6.17. Data points from measurements with two different photon energies $\hbar\omega$ are plotted in the gap of the projected bulk bands (shaded). The inset gives the location in reciprocal space [6.17]

6.4.2 d-like Surface States

In transition metals, *d* orbitals of the single atoms interact in the crystal to give *d* bands which are typically 4–10 eV wide. Due to their localized nature the *d* bands show less dispersion than *sp* bands; they cross and hybridize with the "free electron" *sp* band. This hybridization introduces new gaps in the band structure where true surface states can occur.

Figure 6.20 shows ARUPS data measured on Cu(100). As a function of detection angle the *d*-band emission between 2 and 4 eV binding energy below E_F undergoes considerable changes. In particular, a peak on top of the *d*-band, is recognized as being a surface-state band according to the arguments in Sect. 6.32. The resulting 2D dispersion curve for this band is plotted in Fig. 6.21 along the $\overline{\Gamma M}$ line of the Brillouin zone [6.18]. As expected for a surface-state band, the same dispersion is obtained with different photon energies; furthermore, the states are located in a gap of the projected bulk states. The energetic location close to the higher-lying bulk *d*-states clearly reveals that the band is split off from these bulk *d*-states.

In contrast to Cu, Ag and Au the metals Mo, W, Ni, Pt, etc. have only partially occupied *d* states. Their *d*-band is therefore cut by the Fermi energy E_F (Fig. 6.22). Such relatively localized *d*-band states can be treated theoretically by LCAO type calculations [6.20]. In addition to yielding complete band structures mapped onto the 2D Brillouin zone, one also obtains the so-called *Local Density Of States* (LDOS). This is the total density of states (integral over $k_\parallel$ space) within a certain layer of atoms. The LDOS of the topmost atomic layer thus reflects the density of surface states whereas the LDOS of deeper layers becomes identical to the density of bulk states. The results of such LDOS calculations are exhibited for W(100) in Fig. 6.22. Even the second- and third-layer densities very closely resemble the bulk density of states; the same valley in the state distribution can be seen around E_F. For the topmost layer, however, a relatively sharp structure, half filled, half empty is observed at E_F. The origin of this surface-state band can be described qualitatively as a splitting off of more atomic-like *d*-states from the bulk-state distribution. Surface atoms have fewer neighbors and their electronic structure is therefore closer to that of a free atom than for atoms deep in the bulk. Figure 6.23 displays part of

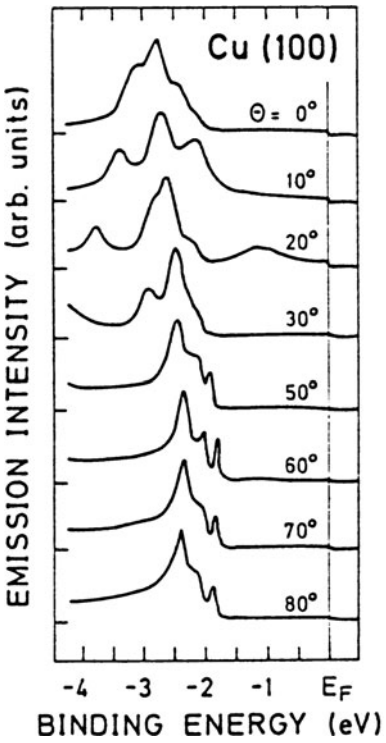

Fig. 6.20 Angle-resolved UV-photoemission curves measured with a photon energy of 21.22 eV on Cu(100) at different detection angles. The emission direction is in the (001) mirror plane containing the symmetry points Γ, X, W and K of the Brillouin zone [6.18]

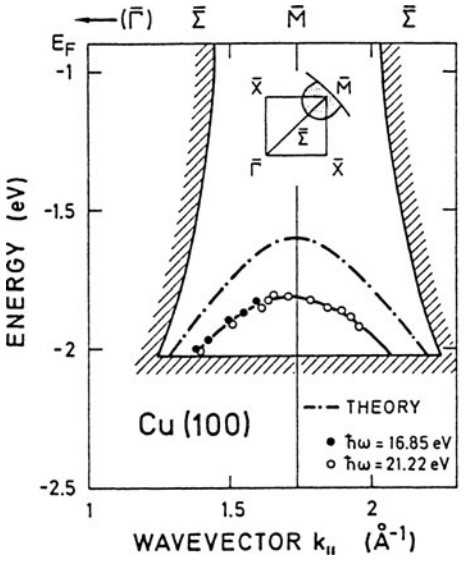

Fig. 6.21 Dispersion of the d-derived surface-state band on Cu(100) according to the ARUPS data of Fig. 6.20. Data points from measurements with two different photon energies $\hbar\omega$ are plotted in the gap of the projected bulk sd bands (bounded by the shaded region). The inset gives the location in reciprocal space. The dashed-dotted curve results from a surface-state band calculation according to [6.18, 6.19]

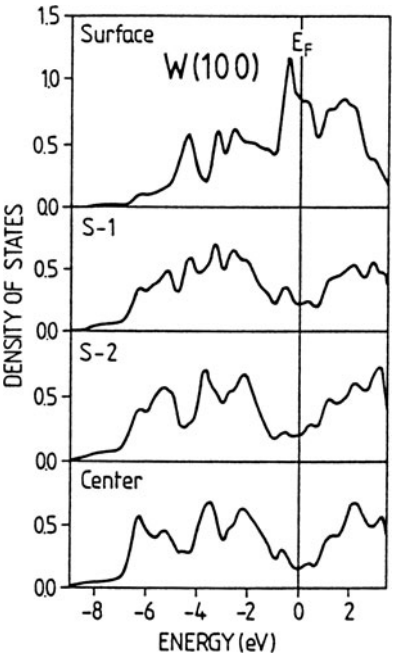

Fig. 6.22 Layer-resolved Local Density Of States (LDOS) for W(100) as obtained by a slab calculation. For the topmost surface atomic layer surface states around the Fermi level E_F produce a strong band in an energy region where, in the bulk LDOS (center layer below), low density is found [6.20]

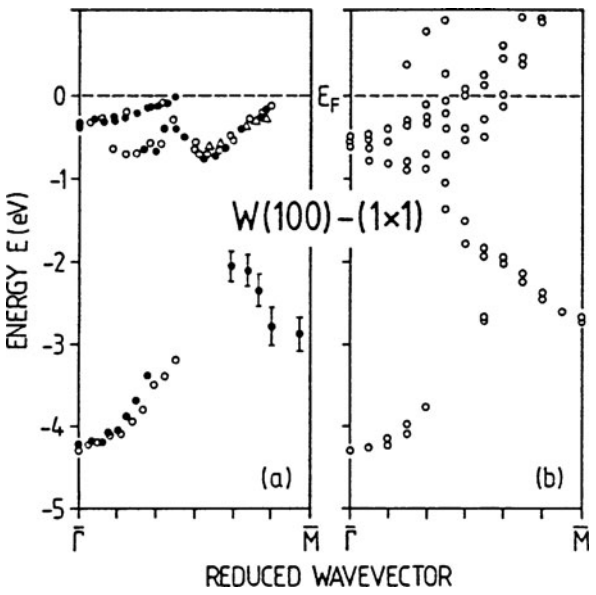

Fig. 6.23 a,b Surface state bands on the W(100) surface with (1 × 1) reconstruction [6.14]. (**a**) Experimental angle-resolved UPS data [6.21, 6.22]. (**b**) Theoretical results from a slab calculation [6.23]

the calculated surface-band structure for W(100) in comparison with experimental results from ARUPS. There are several surface-state bands of d character which contribute to the sharp structure around E_F in Fig. 6.22.

The fact that surface atoms have fewer neighbors than bulk atoms leads, in a LCAO picture for the d-states, to the immediate conclusion that these states have less overlap with neighbors and that the d-LDOS for the topmost atomic layer should be sharper than for deeper layers. A calculation for the d-states on a Cu{001} slab clearly shows this effect (Fig. 6.24). As for W(100) the second atomic layer already exhibits a bulk-like LDOS, whereas at the surface the d band has become considerably sharper. The effect is also clearly revealed in experimental photoemission data (Fig. 6.25).

The narrowing of the d band in the LDOS of surface atoms has further interesting consequences. Because of the small screening length (high electron density) in metals, atoms at the surface tend to remain neutral. Furthermore, one and the same Fermi level must be found in the bulk and in the topmost atomic layer. In order to retain local charge neutrality, shifts of the local band structure are expected and will be reflected in the surface LDOS (Fig. 6.26). For metals whose d-band is less than half full, one expects a downward shift of the electronic levels at the surface. On contrast, an upward shift should occur for metals, whose d-bands are occupied by more than five electrons per atom. These characteristic shifts are also expected for the sharp core levels and should therefore be observable in XPS; but an experimental confirmation is difficult because of the many-body effects involved in interpreting the data (Sect. 6.3.4).

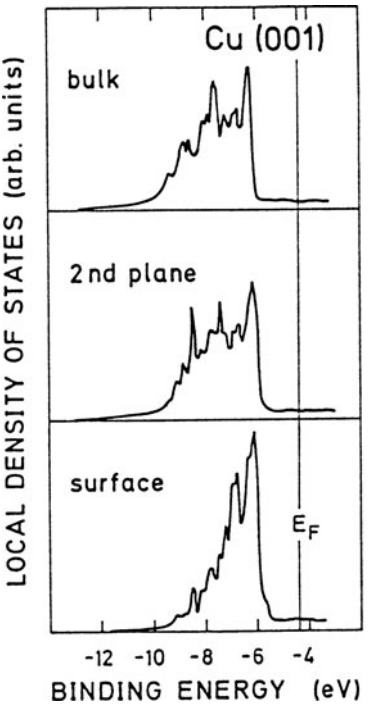

Fig. 6.24 Layer-resolved Local Density Of d-States (LDOS) for the Cu(001) surface obtained from a slab calculation [6.24]

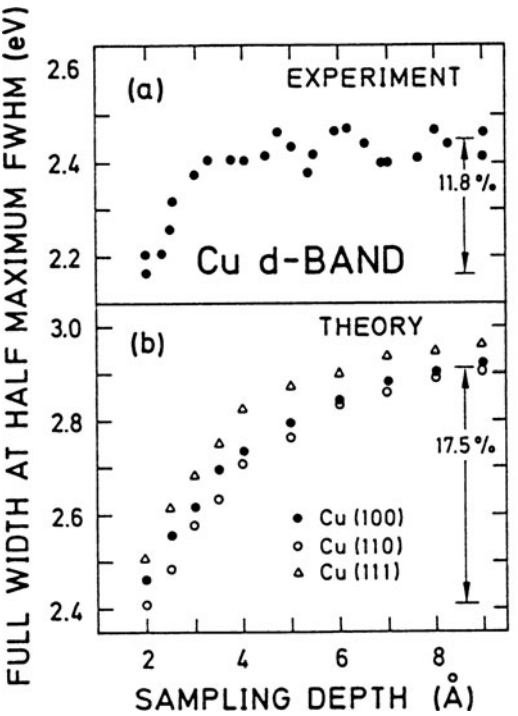

Fig. 6.25 a,b Full Width at Half Maximum (FWHM) of the Cu d-band as a function of depth into the crystal [6.25]. (**a**) Experimental data from photoemission measurements with different photon energies sampling over areas of different depth. (**b**) Results from theoretical calculations for various Cu surfaces

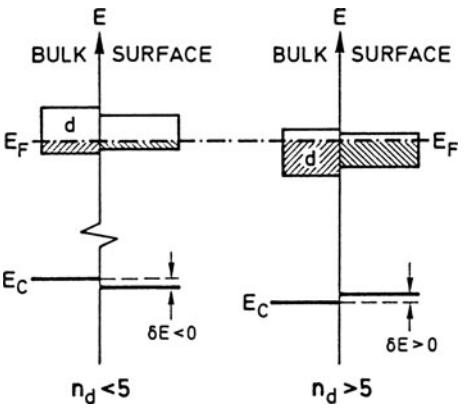

Fig. 6.26 Schematic illustration of the origin of surface corelevel shifts δE in d-band metals. The integer n_d denotes the number of electrons in the band. At the very surface the d-band is narrowed due to the reduced interaction with neighbors. Because of neutrality requirements this leads to shifts of the core level E_c in the topmost atomic layer [6.26]

6.4.3 Empty and Image-Potential Surface States

The importance of photoemission spectroscopy, particularly UPS, for the study of occupied surface states has its analogue in momentum resolved inverse photoemission (Panel XI: Chap. 6), which is similarly useful for the investigation of empty surface-state bands located at energies above the Fermi level E_F. The experimental technique involves the capture of irradiated electrons of a certain kinetic energy in

empty states with simultaneous emission of UV photons of the corresponding deexcitation energy. The energetic position of the particular empty state is obtained from the kinetic energy of the incident primary electrons and the energy of the emitted UV photon. The $\boldsymbol{k}_{\parallel}$ vector of the empty state is determined from the energy and the angle of incidence of the primary electron beam.

The underlying physical process is the inverse (time-reversed) photoeffect. The theoretical treatment is thus similar to that of UPS (Sect. 6.3). In particular, one faces the same problems as in ARUPS in distinguishing between bulk and 2D surface-state bands (Sect. 6.3.2). As in ARUPS, criteria for surface-state bands are: (i) sensitivity to contamination, (ii) energetic position within a gap of the projected bulk band-structure of empty states, and (iii) dependence only on $\boldsymbol{k}_{\parallel}$ and not on $\boldsymbol{k}_{\perp}$. Using these criteria inverse photoemission has meanwhile yielded a number of interesting experimental results about empty surface-state bands on solid surfaces.

Figure 6.27 shows examples of empty surface-state bands which have been measured on the (110) surfaces of Ni, Cu and Ag along the symmetry lines $\overline{\Gamma X}$ and $\overline{\Gamma Y}$ [6.27]. The energy scale is referred to the Fermi level E_{F}, and the vacuum energy E_{vac} is marked by an arrow. In the case of Cu(110) the occupied surface-state band around $\overline{Y}$ and slightly below E_{F} is the same band as appears in Fig. 6.19 (Sect. 6.4.1). In addition to the empty surface-state bands S_1–S_4, one also observes some empty bulk bands (B). The surface-state bands S_2–S_4 show the expected behavior, in particular they are very sensitive to contamination. They can be understood similarly to the occupied bands (Sect. 6.4.1) as being split off from the empty bulk sp-bands. Correspondingly, theories of the type described in Sects. 6.1 and 6.2 are able to reproduce these surface-state bands to within an accuracy of better than 1 eV. This is not the case for the states marked S_1 in Fig. 6.27. In particular, adsorption of chlorine does not lead to the disappearance of the corresponding spectral features in the inverse photoemission spectra. This is shown for a Cu(100) surface in Fig. 6.28. Rather than disappearing, the spectral step near 4 eV above E_{F} shifts by 1.1 eV to even higher energies after the adsorption of Cl[c(2 × 2) superstructure in LEED]. The shift of 1.1 eV is exactly the work-function change due to the adsorbed Cl. The structure S_1, which from its $\boldsymbol{k}_{\parallel}$ dependence and its energetic location in a bulk-band gap is clearly due to surface states, thus shifts in energy as the vacuum level E_{vac} does. This is different from the behaviour of the surface states which are considered so far. All those states were "crystal derived", they are fixed (sometimes as split-off states) to the bulk-band structure rather than to the vacuum level E_{vac} which changes its position with respect to the bulk bands due to the slightest contamination.

The extraordinary behavior of the states designated S_1 in Fig. 6.27 is explained in terms of so-called *image-potential states*. The physical origin of this new type of empty surface state is explained in Fig. 6.29. These states are not derived in any way from bulk states or from the symmetry-breaking effect of the surface. When an electron approaches a metal surface, its charge is screened by the conduction electrons of the metal. The screening can be described in terms of a positive image charge inside the metal at the same distance from the surface as the real charge outside. This leads to an attractive potential between the electron and its positive

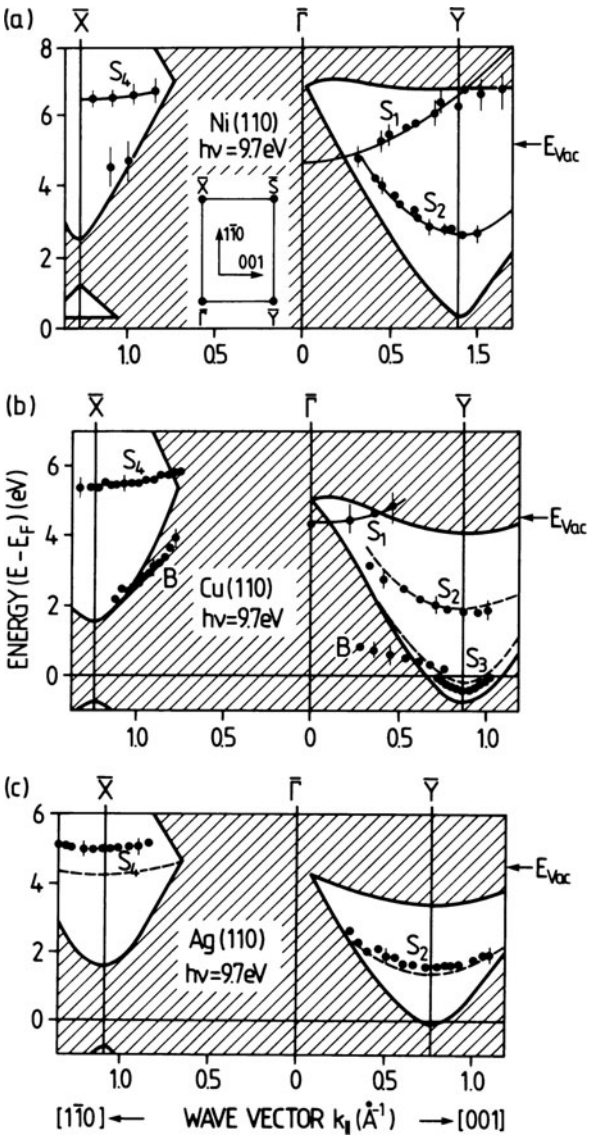

Fig. 6.27 a–b Dispersion of empty surface-state bands S_1–S_4 on the (110) surfaces of Ni, Cu and Ag along the symmetry lines $\overline{\Gamma X}$ and $\overline{\Gamma Y}$. Bulk bands are denoted by B. The energy scale is referred to the Fermi level E_F and the vacuum energy E_{vac} is marked by an arrow. The experimental data originate from inverse photoemission experiments [6.27]

image inside the metal. In the simplest approximation this potential has the Coulomb form

$$V(z) \propto 1/z, \quad z > 0. \tag{6.36}$$

As is shown in Fig. 6.29, it is possible for bound states to exist in such a potential which can thus trap electrons in a region within a couple of Å of the surface. If the energy levels of such states ($n = 1$ in Fig. 6.29) fall into a gap of the bulk-band

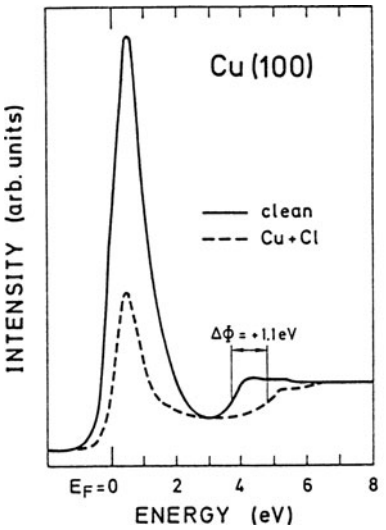

Fig. 6.28 Inverse photoemission (isochromate) spectrum on a Cu(100) surface, clean (full line) and after adsorption of chlorine (broken line). The energy scale extends from the Fermi level E_F up towards the vacuum level [6.28]

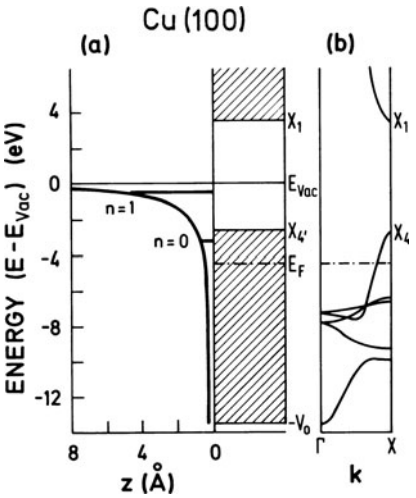

Fig. 6.29 Schematic illustration (**a**) of the origin of image potential surface states for the example of Cu(100). The bulk-band structure of Cu (**b**) gives rise to a gap between $X_{4'}$, and X_1 above the Fermi energy E_F. An electron approaching the surface can be captured by its image potential in one of the quantized states ($n = 0, 1, \ldots$). Trapping in this state occurs when, due to a gap of the empty bulk states, no decay into bulk states can occur [6.28]

structure, the states cannot decay into bulk states and the general behavior of electrons occupying such levels is similar to that of ordinary crystal derived states. The energy of an electron trapped in such an image state is given by the binding energy ϵ_n of the bound state with the quantum number n. The exact value of ϵ_n is determined by the shape of the potential (6.36). Parallel to the surface the electrons are nearly free, i.e. they can move as free electrons and carry a kinetic energy $\hbar^2 k_\parallel^2 / 2m^*$, m^* being their effective mass parallel to the surface. The relevant energy reference for these states is the energy of an electron far away from the surface, i.e. the vacuum energy E_{vac}. One thus arrives at the following description for the band structure of image potential surface states:

$$E(\boldsymbol{k}_{||}) = \frac{\hbar^2 k_{||}^2}{2m^*} - \epsilon_n + e\phi \tag{6.37}$$

where the work function term ϕ takes into account the reference energy E_{vac}. The description (6.37) is consistent with the experimental shift due to adsorption (Fig. 6.28). Furthermore, the parabolic dependence on $k_{\|}$ (6.37) is also found in the experimental data (Fig. 6.27).

It should be stressed that electrons bound in such image potential states form a quasi-2D electron gas. The very interesting properties of such 2D electron gases can be studied more easily in cases where they are formed in thermodynamic equilibrium rather than in excited states as in the present case. A further treatment of such 2D gases is given in connection with semiconductor space charge layers, where such effects are also important (Chaps. 7 and 8).

6.5 Surface States on Semiconductors

Electronic surface states or, more generally speaking, interface states were first studied on semiconductors [6.29, 6.30]. Their existence was derived in an indirect manner by analysing the physics underlying the rectifying action of metal-semiconductor junctions (Chap. 8). An important breakthrough on the experimental front was due to optical experiments [6.30] and to the application of photoconductivity and surface photovoltage spectroscopy [6.31] (Panel XI: Chap. 7). As is the case for metal surfaces, the most detailed information is obtained from UPS [6.32] and ARUPS (Sect. 6.3), inverse photoemission spectroscopy (Panel XI: Chap. 6), from electron-energy loss spectroscopy (Panel IX: Chap. 4) and from STM (Panel VI). The two last of these techniques can give information about excitation energies between occupied and empty surface states, as does optical absorption spectroscopy. In the following we will consider some experimental and theoretical results on low-index surfaces of elemental (Si, Ge) and III-V compound semiconductors (GaAs, InP, InSb, etc.). ZnO will also be considered briefly as an example of the II-VI compounds. The main common characteristics of these different semiconductor classes is the tetrahedral atomic bonding, i.e. the coordination of each atom by four other atoms (of the same kind for Si and Ge and of different kind in compound semiconductors). This tetrahedral bonding geometry results from the formation of the covalent sp^3 hybrids. This covalent part of the bond is the decisive factor for the crystal structure even in the presence of relatively strong ionic bonding contributions as found in II-V compounds such as ZnO. The sp^3 hybridization causes the elemental semiconductors to crystallize in the diamond structure (two fcc lattices mutually displaced by (1/4, 1/4, 1/4) of a unit cell) and the III-V compound materials in the zincblende structure (a diamond structure in which nearest neighbors are atoms of different kinds). Many II-VI crystals occur in the wurtzite structure, which is hexagonal but similar to a slightly deformed zincblende structure [tilted and elongated along (111)].

In Fig. 6.30 the three lowest-index surfaces of the zincblende structure are displayed. The diamond lattice is obtained if all the atoms are of one species. The sp^3 hybridization leads to the formation of strongly directional bonding lobes which appear as *dangling bond* orbitals at the surface. The different dangling bond structures for the three surfaces (assumed to be non-reconstructed, truncated bulk) is shown in Fig. 6.30b. The corresponding 2D Brillouin zones of the non-reconstructed surfaces are depicted in Fig. 6.30c. Formation of the *truncated* (111) surface creates one half-filled dangling bond orbital per surface atom perpendicular to the surface. On the (110) surface there are two atoms in the unit mesh, each with a tilted dangling bond orbital. The unreconstructed (100) surface unit cell contains one atom with two broken bonds tilted with respect to one another. Nature, however, is not as simple as indicated in Fig. 6.30: The main low-index surfaces of all important semiconductors display a variety of complicated reconstructions which are only partially understood.

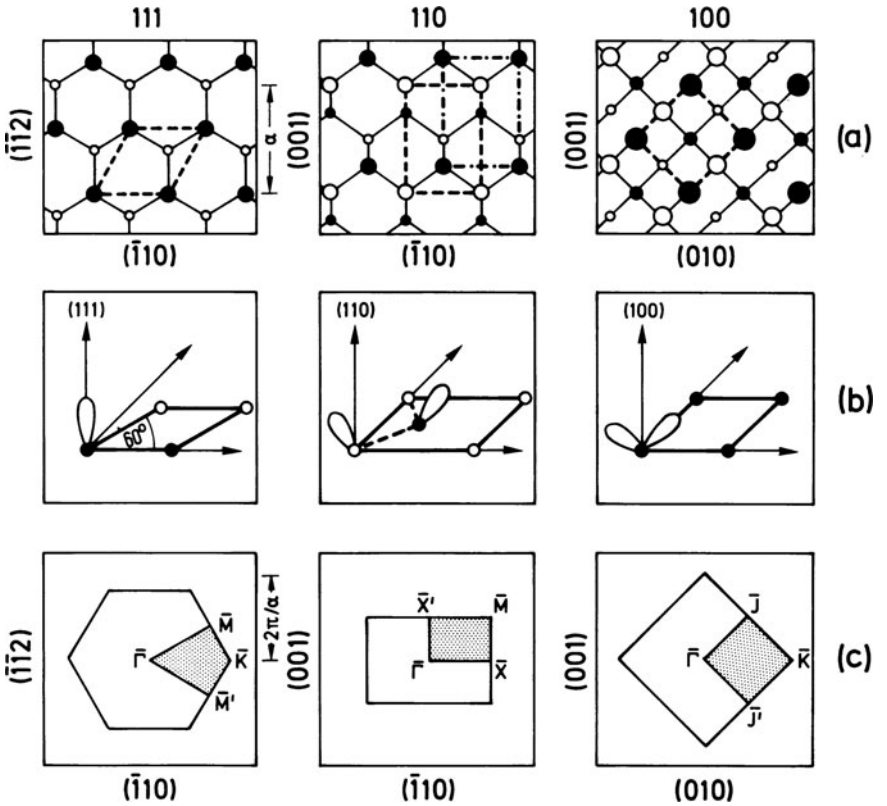

Fig. 6.30 a–c Crystallography of the non-reconstructed three low-index surfaces of the zincblende lattice (sp^3-bonded). The diamond lattice of Si and Ge would be obtained if all atoms were of the same species. (**a**) Top view, smaller symbols denote deeper lying atoms. Possible unit meshs are indicated by broken lines. (**b**) Schematic plot of the dangling-bond orbitals occurring on the different surfaces. (**c**) Corresponding ideal surface Brillouin zone with conventional labeling [6.33]

The few cases for which conclusive reconstruction models have been developed are discussed in the following sections.

6.5.1 Elemental Semiconductors

It is easy to see qualitatively what kind of surface-band structure would result from the local surface geometries (Fig. 6.30) for the three types of unreconstructed surfaces (111), (110) and (100) of Si and Ge. Calculations for Si and Ge based on non-reconstructed surface geometries indeed show the expected behavior (for Ge see Fig. 6.42). Corresponding to the one dangling bond (broken sp^3 bond) on the Ge or Si(111) surface one expects a single band of surface states within the forbidden gap. This band is split off from the bulk sp^3-states forming the valence and conduction bands. Because of the fewer neighbors at the surface, i.e. reduced orbital overlap the surface states are lowered in energy less than the bulk valence-band states and thus fall into the gap. Due to bond breaking the band is half filled since each side of a broken bond can accept one of the two electrons of the unbroken covalent bond. The creation of an ideal (110) surface leaves two dangling bonds on two different atoms in the unit cell. As a result, two dangling-bond surface-state bands are formed in the gap. Since the dangling sp^3 hybrids have only weak mutual interaction, the two bands are only slightly split and exhibit relatively little dispersion. In contrast, the two dangling-bond orbitals on one and the same atom on the (100) surface interact strongly with each other and form two gap state bands spread over a much wider energy range with higher dispersion. In addition to these gap states, all three Si surfaces give rise to so-called *back bond surface states* which lie at much higher binding energies within gaps of the projected bulk band structures. The wave functions of these states are localized between the topmost and lower lying atomic planes.

These simple conclusions concerning the band structure of the unreconstructed surfaces belie the fact that reality is much more complex. This is because of reconstructions. One of the most studied semiconductor surfaces is the *Si(111) cleaved surface*.

If the crystal is cleaved at room temperature, a (2×1) reconstruction is found in LEED. If cleaved at very low temperature ($T < 20\,\mathrm{K}$) a (1×1) LEED pattern appears. After annealing to temperatures higher than about 400°C a (7×7) superstructure occurs indicating an extremely long-range periodicity. The (7×7) structure is definitely the most stable configuration; the (1×1) and the (2×1) structures are frozen-in metastable configurations.

The Si(2×1) surface has attracted much attention in recent years. Independent of the reconstruction model considered, there is an interesting argument that the (2×1) reconstruction splits the half-filled dangling-bond surface-state band within the bulk gap into two parts: according to Fig. 6.31 the 2D Brillouin zone shrinks by a factor of two in one direction for the (2×1) structure i.e., for symmetry reasons, one half of the dangling-bond band can be folded back into the new (2×1) Brillouin zone thus opening up a gap at the (2×1) zone boundary [due to the perturbation

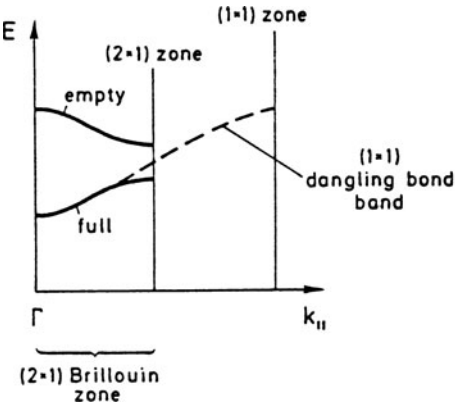

Fig. 6.31 Schematic illustration of the energy gain due to the formation of a (2×1) dangling bond surface reconstruction. The shrinking of the Brillouin-zone dimension by a factor of two in one direction causes the half-filled dangling bond surface state band (broken line) to be folded back into the new (2×1) zone and split at the zone boundary, thus leading to a reduction of the total electronic energy

potential causing the (2×1) reconstruction]. Since the original (1×1) band was half filled, this splitting into an empty upper branch and a full lower branch leads to a total energy decrease and thus to a stabilization of the (2×1) structure. These arguments are reminiscent of a Peierls instability and no detailed assumptions about the reconstruction are necessary.

For a long time the so-called *buckling model* had been assumed to explain the double periodicity along $[\bar{2}11]$ on the cleaved Si(111)-(2×1) surface [6.34] (Figs. 3.6b, Fig. 6.32). Every second row of surface Si atoms is raised with respect to the ideal lattice position and the rows of atoms in between are shifted downwards. As was shown by a number of researchers [6.35] such a reconstruction always yields an empty and an occupied surface state band (as expected, see

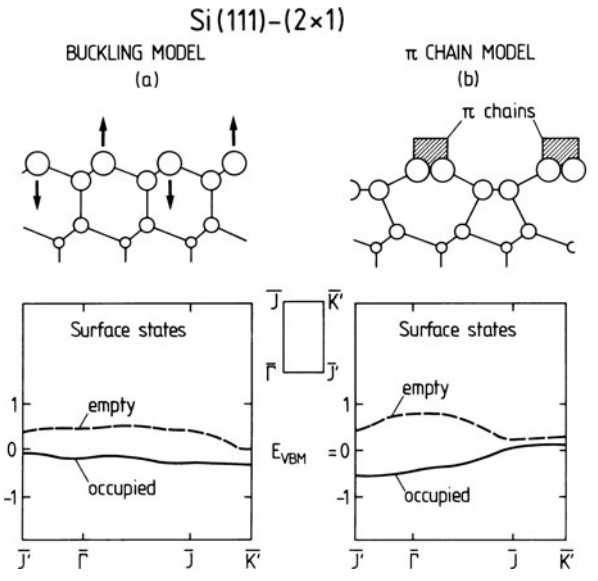

Fig. 6.32 Calculated dispersion of the dangling-bond surface-state bands for Si(111)-(2×1) [6.36] (**a**) for the buckling model shown in the upper part; (**b**) for the π-bonded chain model shown in the upper part. See also Fig. 3.6

above) with little dispersion along the $\overline{\Gamma J}$ symmetry line of the (2×1) surface Brillouin zone (Fig. 6.32a). This is in contradiction to the experimental findings from ARUPS (Fig. 6.33). A number of different groups have experimentally observed strong dispersion along $\overline{\Gamma J}$. This finding, and all other experimental data so far can be explained in terms of the so-called *π-bonded chain model* of Pandey [6.36] (Figs. 3.6, 6.32b). Complete Si–Si bond breaking is required in the second atomic layer to induce this reconstruction. But the resulting zig-zag pattern allows the dangling p_z bonds of the topmost layer to form one-dimensional π bonds just like in a one-dimensional organic system. As has been shown theoretically, in spite of the bond breaking, the π-bonded chain model is energetically more favorable than the buckling model, due to the energy gained by the formation of the π-bonds [6.39]. The strongly dispersing, occupied and empty surface state bands are due to the bonding π-orbitals (without nodes) and the anti-bonding π^* orbitals (with nodes along the chain). If, in addition to the π-bonding, a slight buckling in the topmost atomic layers is included, all available experimental data are well described. In particular, the strong dispersion measured in ARUPS is obtained (Fig. 6.33). There is an absolute gap in the surface-band structure at $\overline{J}$ (Figs. 6.32b, 6.33) with a calculated energy distance between π and π^* bands of less than 0.5 eV. Indeed in High-Resolution Electron Energy Loss Spectroscopy (HREELS) (Fig. 6.34) and in IR multiple internal reflection spectroscopy (Fig. 6.35) the corresponding optical transitions are seen at energies of about 0.45 eV. As is expected for the $\pi \rightarrow \pi^*$ optical transitions (like in an organic chain molecule) there is a strong polarization dependence of the transition matrix element. For light polarized normal to the chains the transition is not excited (Fig. 6.35). The results of this reflection absorption experiment are crucial for the π-bonded chain model, since they cannot be explained by the buckling model. Moreover, the available structural data from LEED and from Rutherford backscatting are in complete agreement with a slightly buckled π-bonded chain

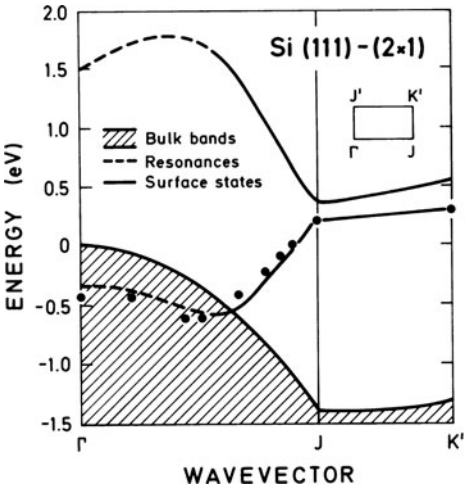

Fig. 6.33 Dispersion of the dangling-bond surface-state bands for the Si(111)-(2×1) surface together with the projected bulk-band structure (shaded). The corresponding symmetry directions in k-space are explained in the inset (surface Brillouin zone). Full and broken curves are the result of theoretical calculations [6.37]. Data points were obtained by ARUPS measurements [6.38]

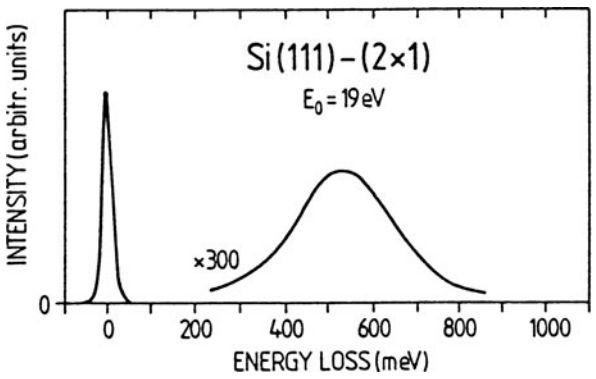

Fig. 6.34 High-Resolution Electron Energy Loss Spectrum (HREELS) of a clean, cleaved Si(111)-(2 × 1) surface for specular reflection (70°) and with a primary energy E_0 of 19 eV [6.40]

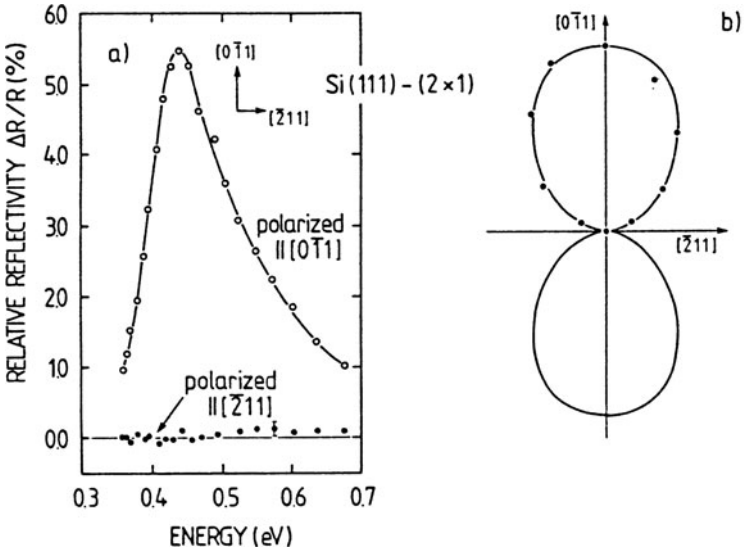

Fig. 6.35 a,b IR multiple internal reflection spectroscopy of the cleaved Si(111)-(2 × 1) surface. (**a**) Relative reflectivity change between a clean and oxygen covered surface for light polarizations parallel to $[0\bar{1}1]$ (π-chain direction) and parallel to $[\bar{2}11]$ (normal to π-chain direction). (**b**) Polar diagram of the relative reflectivity change as a function of light polarization direction [6.41]

model for the Si(111)-(2 × 1) surface. This well established model is now also used to describe the *cleaved Ge(111) surface with* (2 × 1) superstructure. Figure 6.36 shows a comparison of surface state dispersion branches along $\overline{\Gamma J}$ and $\overline{\Gamma K}'$ measured in ARUPS [6.43] with theoretical curves which have been calculated on the basis of a buckled π-bonded chain model [6.42].

The famous *Si(111)-(7 × 7) surface* with its large unit cell is the most stable surface structure on Si(111). It is prepared by annealing a clean (111) surface; the details of the annealing (and ion bombardment) depend on whether the clean surface has been obtained by cleavage (2 × 1 superstructure), sputtering or annealing. A structure model has been proposed by Takayanagi et al. [6.44] on the basis

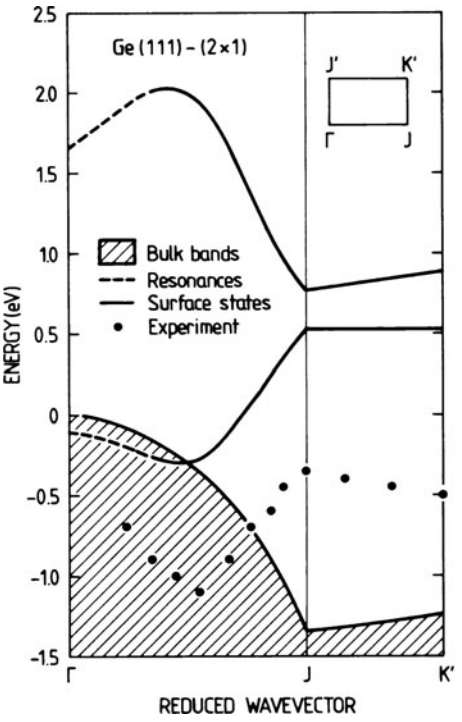

Fig. 6.36 Dispersion of the dangling-bond surface-state bands for the clean, cleaved Ge(111)-(2 × 1) surface together with projected bulk-band structure (shaded). The corresponding symmetry directions are explained in the inset (surface Brillouin zone). Full and broken curves are the results of theoretical calculations [6.42]. Experimental data points were obtained from ARUPS measurements [6.43]

of transmission electron diffraction, which has found further confirmation from Scanning Tunneling Microscopy (STM) and other techniques (Fig. 6.37). This model, referred to as the DAS (Dimer-Adatom Stacking-fault) model contains 12 Si adatoms, 6 rest atoms, 9 dimers and one corner hole per surface unit cell. In one half of the unit cell there is stacking fault which explains the slight asymmetry found in STM (Fig. VI.4, Panel VI: Chap. 3).

To calculate the electronic structure of such a complicated reconstructed surface is an enormous task. Nevertheless some general conclusions about the surface-state density are possible. Using the arguments which were discussed in connection with the Si(111)-(2 × 1) surface (Fig. 6.31) one has a 2D surface Brillouin zone for the (7 × 7) superstructure whose diameter is 1/7 of the (1 × 1) zone, i.e. because of symmetry, the one dangling-bond band of the (1 × 1) non-reconstructed surface (Fig. 6.31) can be folded back seven times into the (7 × 7) Brillouin zone. This procedure is expected to yield a manifold of bands lying close to each other, i.e. a quasi-continuous distribution of states within the forbidden bulk band of Si. Thus a quasi-metallic character is expected for the Si(111)-(7 × 7) surface. A sharp Fermi edge for the surface states has indeed been found by some groups in photoemission spectroscopy [6.45, 6.46]. In HREELS performed on very clean and well-ordered (7 × 7) surfaces, a broad and intense background is found which is attributed to a continuum of electronic transitions between continuously distributed surface states [6.79]. In addition, ARUPS experiments show at least three different surface peaks

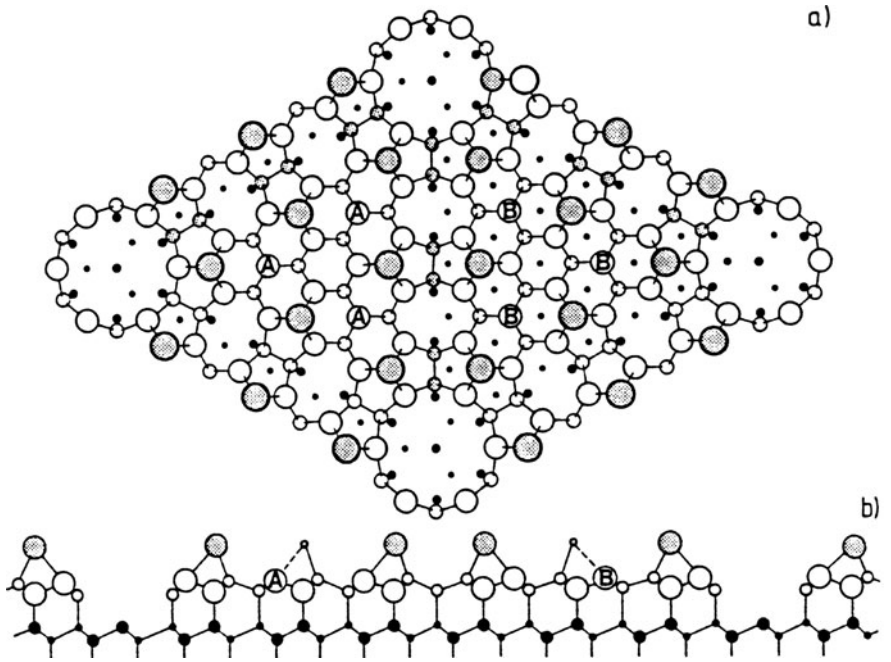

Fig. 6.37 a, b Dimer-Adatom Stacking fault (DAS) model for the Si(111)-(7 × 7) surface. (**a**) Top view: Atoms in (111) layers at increasing depth are indicated by circles of decreasing sizes. The heavy circles represent the 12 adatoms. The circles marked by A and B represent the rest atoms in the faulted and unfaulted half of the unit cell, respectively. (**b**) Side view: Atoms in the lattice plane along the long diagonal of the surface unit cell are shown with larger circles than those behind them [6.44]

above and below the upper valence-band edge (S_1, S_2, S_3 in Fig. 6.38) whose dispersion plotted versus wave vector in the (1 × 1) Brillouin zone is not very significant at least in the wave-vector range considered [6.47]. The surface-state band S_1 might well show some dispersion near the zone boundary and cross the Fermi level. It thus might be responsible for the metallic character of the surface. Inverse photoemission experiments also indicate a continuous distribution of empty surface states in the upper half of the forbidden band with two maxima slightly above the conduction-band edge. Figure 6.39 shows qualitatively the density of both occupied and empty surface states, as derived from UPS and inverse photoemission measurements. The transition marked by $\hbar\omega$ (double arrow) has also been found by means of HREELS measurements [6.50].

For semiconductor devices, the Si(100) is by far the most important surface (Sects. 7.6, 7.7). The clean *Si(100)-(2 × 1) surface* prepared by ion bombardment and annealing has therefore also attracted much interest. The (2 × 1) superstructure could be due to missing surface atoms. But on the basis of UPS data and a calculation of the density of surface states Appelbaum et al. [6.51] were able to rule out such a vacancy model for the Si(100)-(2 × 1) surface (Fig. 6.40a). As is expected

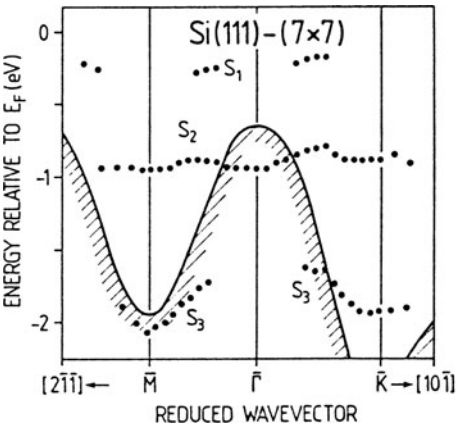

Fig. 6.38 Experimentally determined dispersion of surface state bands (S_1, S_2, S_3) on the clean Si(111)-(7 × 7) surface (points). The projected bulk valence band is indicated by its shaded upper boundary [6.47]

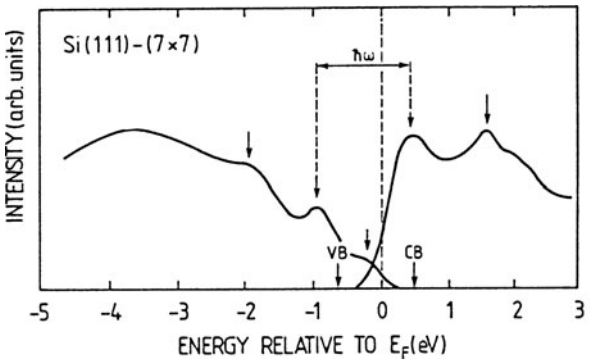

Fig. 6.39 Schematic distribution of occupied and empty surface states of the Si(111)-(7 × 7) surface. The curves are constructed from several sets of experimental data [6.45–6.49]. The arrow marked $\hbar\omega$ represents an electron energy loss observed experimentally. Other tic marks show occupied and empty surface states as revealed by UPS and inverse photoemission experiments [6.50]

from purely geometrical considerations, the sp^3-like dangling bonds on neighboring Si surface atoms could dehybridize into orbitals whose nature is more sp_z, p_x, p_y, and finally form Si dimers at the surface (Fig. 6.40b). According to Fig. 6.30 this dimerization would be in the (110) surface direction. From Fig. 6.40a it is evident that such a dimer model (in contrast to Fig. 6.40b a symmetric dimer) gives better agreement between measured and calculated surface state densities. More detailed investigations show that the symmetric dimer might not be the correct atomic configuration. The asymmetric dimer shown qualitatively in Fig. 6.40b, which is related to a certain degree of ionicity (because of its asymmetry), leads to even lower total energy in the calculation. The dangling-bond band dispersion has been calculated both for the symmetric and the asymmetric dimers (Fig. 6.41c, d). For the asymmetric dimer a total gap between the occupied and empty surface states appears, the surface is thus semiconducting – in contrast to the symmetric dimer surface.

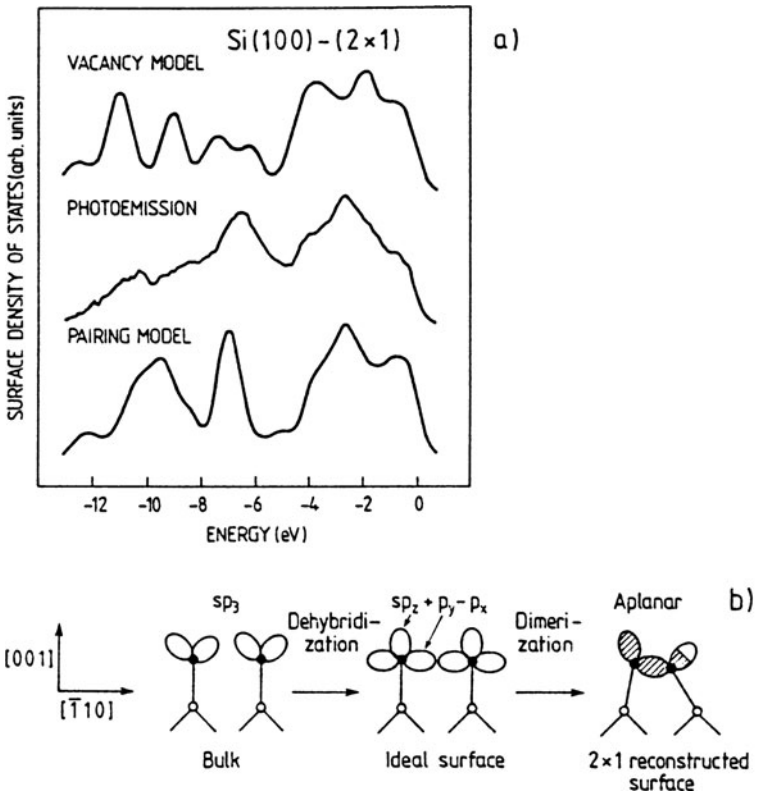

Fig. 6.40 Surface states on Si(100)-(2 × 1) [6.51]. (**a**) Calculated surface densities of states for the Si(100)-(2 × 1) surface for the vacancy and the dimer pairing models as compared to an experimental UV photoemission spectrum ($\hbar\omega = 21.2\,\text{eV}$, true secondaries subtracted). (**b**) Schematic diagram of the dehybridization and dimerization leading to the non-planar dimer structure

A semiconducting surface with essentially no surface-state emission near the Fermi level E_F is found in ARUPS data (Fig. 6.41a). Furthermore the main surface-state band between Γ and J' agrees quite well with the calculated dispersion for the asymmetric dimer model (Fig. 6.41c). Meanwhile there is further experimental support both from ARUPS [6.54, 6.55] and from inverse photoemission (Panel XI) data also for the empty surface states [6.56]. In Fig. 6.41e these data are compared with further theoretical results from surface state-band calculations [6.57]. As far as the earlier results for the asymmetric dimer model in Fig. 6.41a, c are concerned there is good agreement. But in addition to the earlier data there are two bands of occupied surface states (D, D_i, B_2) deep in the bulk valence band region which are attributed to back bonds below the topmost atomic layer. The energetically higher lying surface state band (A) following essentially the contour of the upper bulk valence band edge is explained as in earlier work in terms of dangling bond states. The occupied bands A and B are equally found in the previous work (Fig. 6.41a). Dangling bond states are also responsible for the band of unoccupied surface states

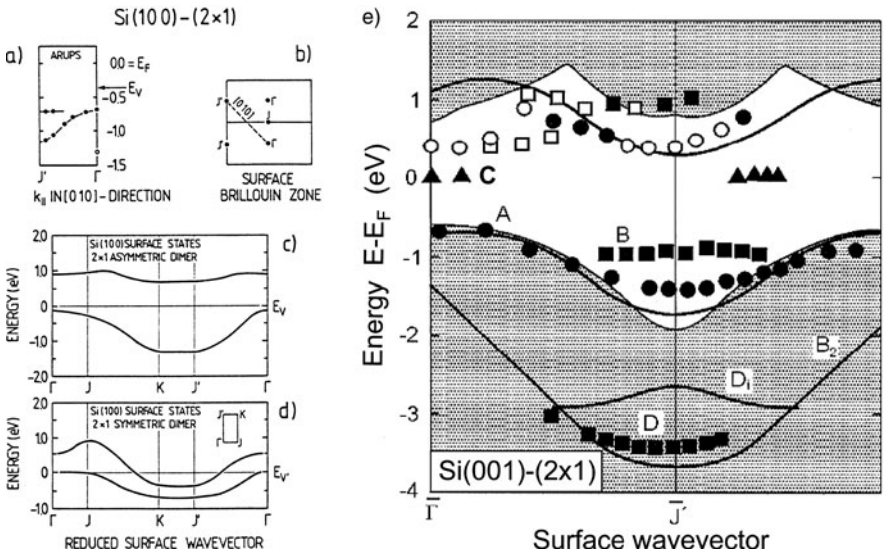

Fig. 6.41 a–e Surface state dispersion on Si(100)-(2 × 1). (**a**) The experimentally determined dispersion from ARUPS [6.52]. (**b**) Surface Brillouin zone showing the orientation of the ARUPS measurement in (**a**). (**c, d**) Calculated dispersion curves for the (2 × 1) asymmetric and the (2 × 1) symmetric dimer models, respectively [6.53]. (**e**) Occupied and empty surface state bands in the [001] direction on single domain Si(001)-(2 × 1) surfaces. The surface state bands D, D_i, and B_2 are attributed to back bonds, while band A is ascribed to dangling bond surface states. Data points below and above the Fermi level are experimental results from Johansson et al. [6.54], Martensson et al. [6.55], and Johansson and Reihl [6.56]. The *curves* in full line are theoretical results by Pollmann et al. [6.57]. The *shaded* areas indicate the surface-projected bulk bands. The compilation of the data is due to Mönch [6.58]

close to the lower bulk conduction band edge [6.56]. In ARUPS surface state bands (C) very close to the Fermi level at the surface, in the midst of the forbidden bulk band, are found [6.55] whose origin is unclear. They might in some way be related to the high doping level of the used Si samples or to defects. Neither the empty surface states at about 0.4 eV above E_F near the $\overline{\Gamma}$ point can be explained so far. The example of the Si(100)-(2 × 1) surface also shows how ARUPS data help to clarify structure models for semiconductor surfaces.

6.5.2 III-V Compound Semiconductors

It is instructive to compare the calculated band structures of the III-V semiconductor GaAs with its isoelectronic neighbor Ge (Fig. 6.42). In the bulk-band structure the essential difference is the opening in GaAs of the so-called *ionicity gap* between −6 and −11 eV. The differences in the surface-state band structure of non-reconstructed GaAs(111), (110) and (100) surfaces are easily understood in terms of the local dangling-bond geometry (Fig. 6.30). Each surface state band of

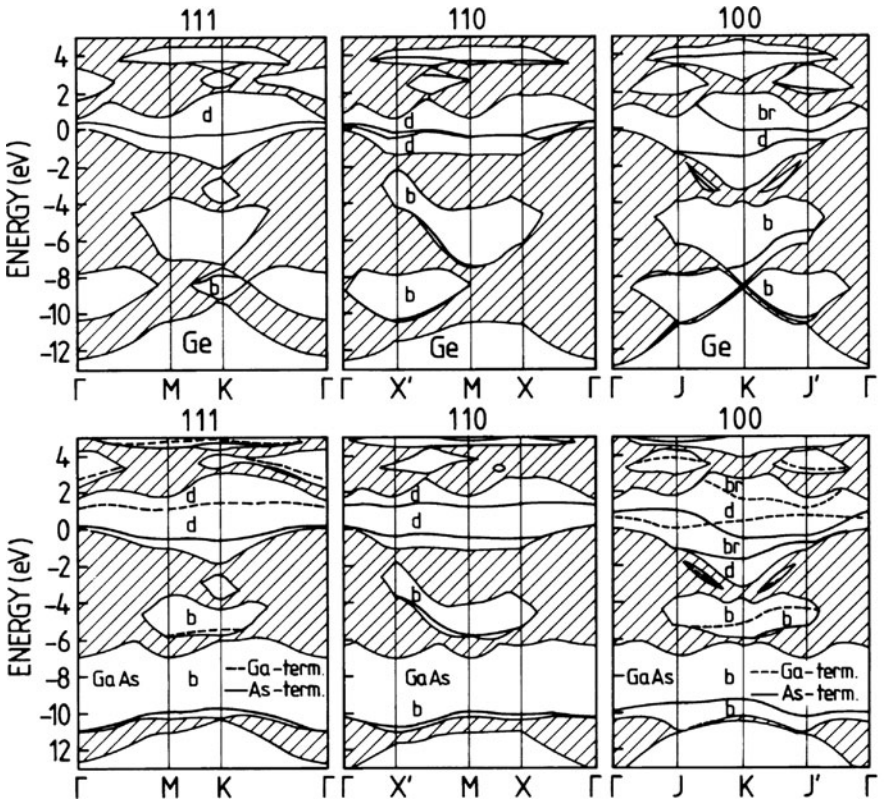

Fig. 6.42 Comparison of calculated surface state band structures of the non-reconstructed low-index surfaces of Ge and GaAs with dangling-bond surface states (d), broken-bond states (br) and back-bonding states (b). For the polar (111) and (100) GaAs surfaces Ga- and As-terminations lead to different surface state bands (broken lines and solid lines, respectively). The projected bulk band structure is shaded [6.59]

Ge splits into a corresponding cation- and anion-derived band in GaAs. The (110) surface is a non-polar surface with equal numbers of Ga- and As-atoms. On the ideal, non-reconstructed (110) surface the anion- and cation-derived surface-state bands lie in the bulk gap (Fig. 6.42). According to the nature of the bulk conduction and valence-band states, the low-lying band (near E_V) is As and the high lying band (near E_C) Ga derived. The (111) and (100) surfaces are polar surfaces, which can be either Ga or As terminated. In reality, the type of termination can, to a large extent be controlled during growth by the beam flux in MBE (Sect. 2.4). The As-terminated surface is generally more stable, since a Ga excess easily leads to Ga aggregation and segregation. In the surface-state band schemes one observes As- or Ga-derived bands depending on the termination (Fig. 6.42).

As in the case of elemental semiconductors, III-V semiconductor surfaces also reconstruct and the surface-state bands cannot be derived as easily as in Fig. 6.42. In

fact, the experimental investigation of surface-state band structure, e.g. by ARUPS, often helps one to construct and experimentally verify surface structure models.

Of the III-V semiconductor surfaces the *GaAs(110) surface* prepared by cleavage in UHV is certainly the most thoroughly studied. From careful measurements of the work function (Panel XV: Chap. 9) for different bulk dopings [6.61] and from a number of photoemission studies, it is well known that on a perfectly cleaved surface with mirror-like finish, the Fermi level is not pinned (Sect. 7.7); the bulk-band gap should essentially be free of surface states. On the other hand, according to Fig. 6.42 and the calculations of a number of other groups (Fig. 6.43a) an unreconstructed (110) surface with atomic positions as in the bulk always gives Ga and As derived

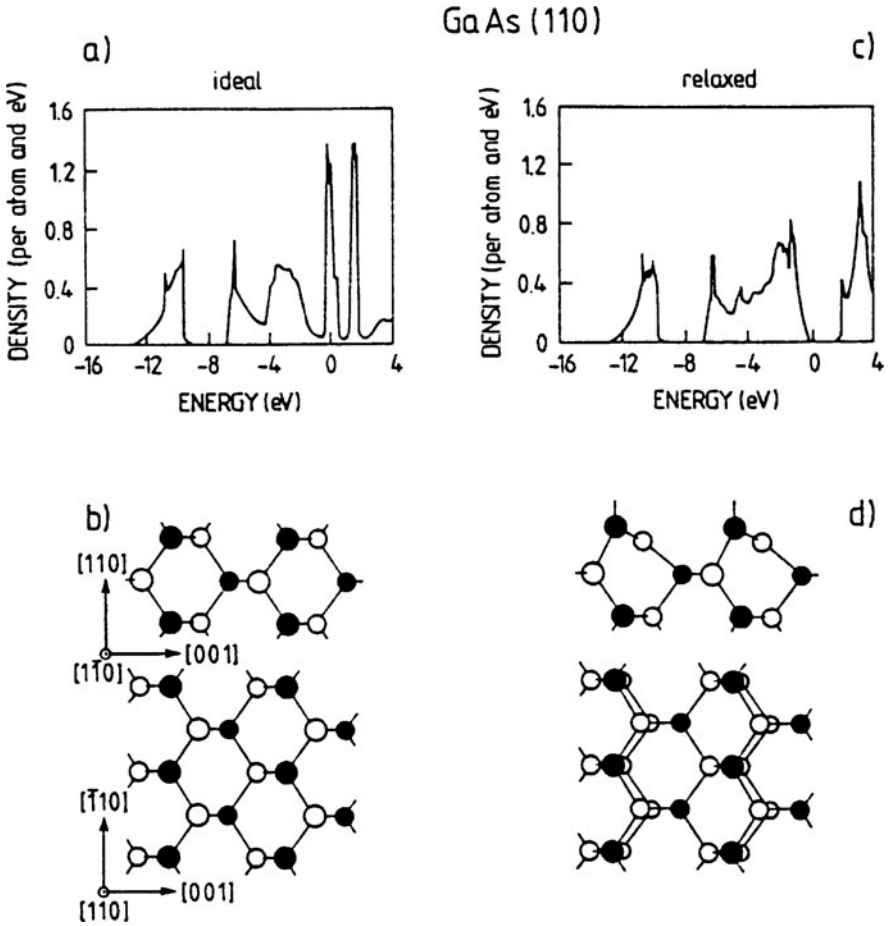

Fig. 6.43 a–d Surface state densities and the corresponding structure models for the GaAs(110) surface. (**a, c**) Calculated surface state densities for the ideal, non-reconstructed (left) and the relaxed (right) surface. The zero of the energy scale is taken to be the upper valence band edge, $E_v = 0$. (**b,d**) Structure models (side and top view) for the ideal, non-reconstructed (left) and the relaxed (right) surface [6.60]

dangling-bond states within the gap, the Ga derived acceptor-like states near midgap and As derived donor states in the lower half of the forbidden gap (Fig. 6.43a). The latter states could not be detected in UPS. On the basis of LEED intensity analyses and Rutherford backscattering data, the reconstruction model of Fig. 6.43d was developed, in which the topmost As atoms are displaced outwards and the neighboring Ga atoms inwards with respect to their unreconstructed bulk-like position (Sect. 3.2). The best structure model achieved so far is described by a rotation of the atoms in the top layer by 27° and a contraction of the first interlayer distance by 0.05 Å. This atomic arrangement on a cleaved GaAs(110) surface indicates a dehybridization of the sp^3 tetrahedral bonds. The trivalent Ga adopts almost planar sp^2-bonds, while the As atom tends to a pyramidal $AsGa_3$ configuration with bond angles close to 90° and having more p-like character. This dehybridization is thought to be connected with a charge transfer from the Ga to the As surface atom. The Ga dangling bonds are emptied and the As states are occupied. This picture of the charge transfer is in agreement with core level shifts observed in XPS (Fig. 8.16). Note, however, that this reconstruction – a so-called *relaxed surface* with a (1 × 1) LEED pattern (Fig. 6.43d) – shifts the dangling bond surface states out of the bulk-band gap (Fig. 6.43c).

Furthermore, there is good agreement between the calculated surface state-band structure for a relaxed surface and the dispersion of surface states measured in ARUPS (Fig. 6.44). As may also be derived from Fig. 6.43a,c this agreement cannot be obtained for an unrelaxed surface. Inverse photoemission spectroscopy (isochromate mode) (Panel XI: Chap. 6) was used to measure the density of empty surface states on a clean GaAs(110) surface, which was prepared by ion bombardment and annealing in UHV. The isochromate spectrum of Fig. 6.45 clearly shows the empty, Ga-derived surface states to be degenerate with conduction-band states. The gap is free of states, as is required by the calculation for the relaxed surface (Fig. 6.43c).

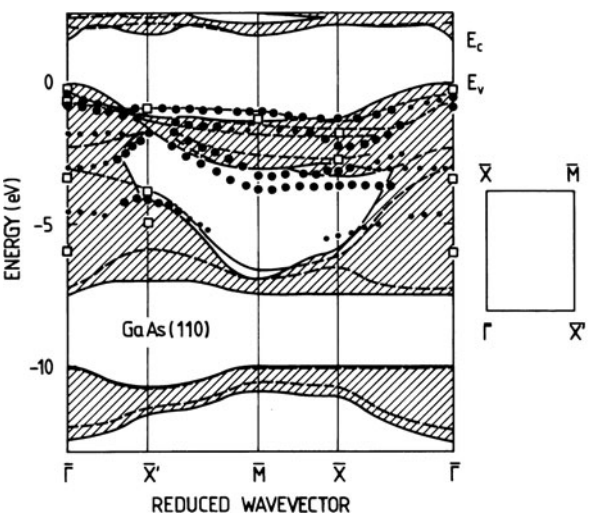

Fig. 6.44 Measured and calculated dispersion curves of surface states (solid lines) and surface resonances (dashed lines) on cleaved GaAs(110) surfaces along the symmetry lines of the surface Brillouin zone (right-hand side). The shaded areas represent the projected bulk band structure. (Calculation from [6.57], experimental ARUPS data from [6.63] (□) and [6.64] (•)

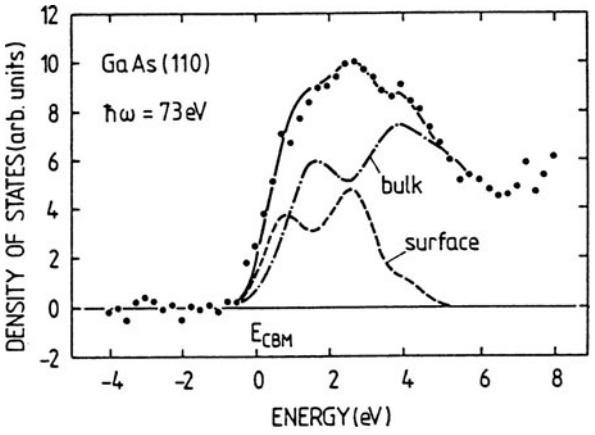

Fig. 6.45 Inverse photoemission (isochromate) spectrum of empty bulk and surface states on a GaAs(110) surface prepared by ion bombardment and annealing in UHV. The solid line is the total density of states above the conduction band minimum E_{CBM} at the surface. The surface and the bulk contributions are shown as dashed and dash-dotted lines, respectively [6.65]

In this context, it is remarkable that the same type of reconstruction (Fig. 6.43d) is obviously present on both the cleaved, as well as the ion-bombarded and annealed (110) surface. This conclusion also follows from LEED intensity analyses. Nevertheless, these differently prepared (110) surfaces differ in their electrical properties. On ion-bombarded surfaces, space charge layers are always observed due to the presence of defect-derived surface states (Sect. 7.6).

Only the (110) surface of GaAs can be prepared by cleavage. The other surfaces require ion-bombardment and annealing or MBE, the latter producing better-defined surfaces (Sects. 2.4, 2.5). Among the low-index surfaces *GaAs(001)* can be prepared in MBE with a number of different superstructures, depending on details of the As/Ga flux ratio, substrate temperature, etc. A particularly stable surface is the As-stabilized surface with its (2×4) superstructure, which is prepared at 800 K and an As_4/Ga flux ratio of about 10/1 [6.66]. The 2D surface band structure of this GaAs(001) (2×4) surface has been measured by ARUPS [6.66]; the bands of occupied states are shown in Fig. 6.46a. The four-fold periodicity along the (110) direction for the (2×4) reconstruction was not observed. The experimental data are therefore plotted with respect to a (2×1) Brillouin zone in Fig. 6.46. The relation of the (2×1) to the (2×4) Brillouin zone is explained in Fig. 6.46b. A detailed comparison with theoretical dispersion curves having the four-fold symmetry is thus difficult. On the basis of a theoretical (2×1) reconstructed dimer model, the low lying surface state band S_4 near -3 eV binding energy is attributed to As–As dimer bonding states. From these results one can infer that As–As dimers, similar to the Si–Si dimers on Si(100)-(2×1) (Fig. 6.40b), are the building blocks of the As-rich GaAs(001)-(2×4) surface.

It is assumed at present that many of the features of the GaAs(110) and (001) surfaces discussed here also apply to other III-V compound semiconductors [6.63]. A number of studies have revealed similarities between GaAs, InP and InSb. P–P dimers, for example, play a similar role on InP surfaces as do As–As dimers on GaAs. On the other hand, there are also some important differences; for example,

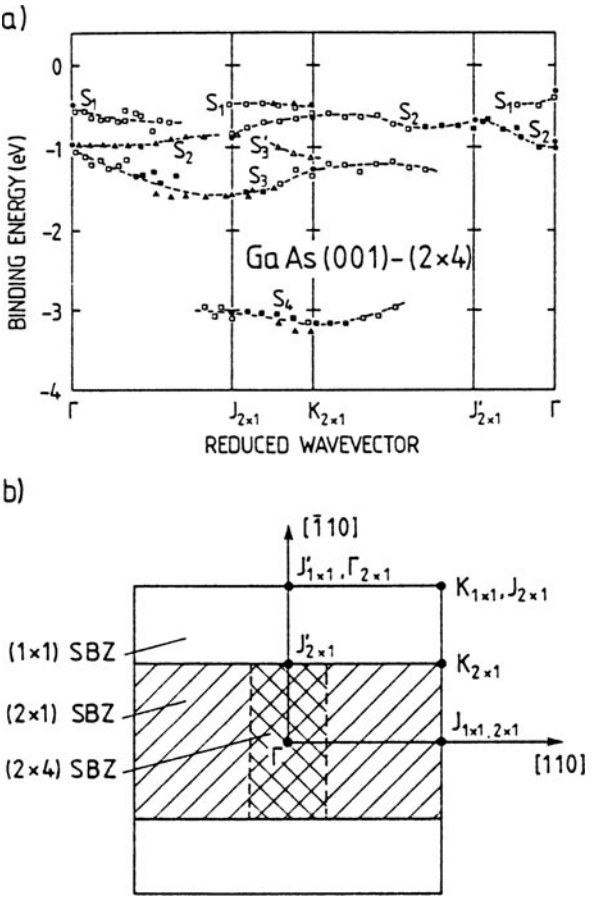

Fig. 6.46 Measured dispersion curves (**a**) of surface states on the As-stabilized GaAs(001)-(2 × 4) surface along symmetry lines of a (2 × 1) surface Brillouin zone (**b**) [6.66]

on well-cleaved GaP(110) surfaces, the Ga derived empty surfaces states lie in the bulk gap, in contrast to those of GaAs(110).

The narrow gap semiconductors InAs ($E_g \approx 340$ meV) and InSb ($E_g \approx 180$ meV) – we will see in the next section – and also InN are insofar similar to GaAs that their nonpolar surfaces with perfect finish show reconstructions as the GaAs(110) surface in Fig. 6.43d, where the group V atom is displaced outward and the neighboring group III atom inward with respect to their unreconstructed bulk-like position. This reconstruction obviously causes a shift of the donor-type and acceptor-type surface state bands out of the bulk forbidden band. In the case of narrow gap semiconductors, hereby, the narrow direct Γ gap with its low conduction band state density is not relevant but rather the indirect gap between the valence band maximum and the side conduction band minimum with its high density of states. This will be discussed in more detail in connection with space charge layers on semiconductor surfaces and surface potentials in Sect. 7.7.

6.5.3 Group III Nitrides

Even though the group III nitrides AlN, GaN, InN and their ternary and quaternary alloys are in principle III–V semiconductors, these compounds differ in many respects from the classical III–V materials. Their most stable crystal structure is that of the wurtzite lattice, but also the less stable cubic zincblende structure of GaAs does exist (Fig. 6.47). The wurtzite lattice has hexagonal symmetry with the *c*-axis perpendicular to the (0001) basal plane of the lattice. Along this *c*-axis the wurtzite lattice resembles the zincblende lattice of GaAs when seen along the [111] direction. In these two directions the crystals contain a stacking sequence of atomic bilayers consisting of two closely packed hexagonal layers orthogonal to the *c*-axis or the [111] direction, one with cations and the other with anions. Crystal surfaces perpendicular to the *c*-axis have either a cation polarity (0001) or an anion polarity $(000\bar{1})$. Correspondingly a GaN basal surface is either Ga(0001) or N$(000\bar{1})$ terminated. The polarity of the semiconductor film depends on the choice of the substrate used for the epitaxial growth (Si, SiC, Al_2O_3, etc.). These polar surfaces can only be prepared by epitaxy or by mechanical cutting and subsequent cleaning in UHV. In contrast, the nonpolar surfaces $(1\bar{1}00)$ and $(11\bar{2}0)$ can be prepared by cleavage in UHV as does the GaAs(110) surface (Fig. 6.48). The GaN$(1\bar{1}00)$ surface is most similar to the GaAs(110) surface. Perfectly cleaved in UHV, it shows a (1×1) reconstruction similar to GaAs(110) in Fig. 6.43d. The Ga atoms are moved inward by about 0.029 nm while the N atoms do almost not change their position with respect to the truncated bulk.

Concerning electronic surface states we therefore must consider several types of surfaces, where also the detailed preparation processes may have a considerable effect on the surface state distribution. An example for an ARUPS study of the Ga-terminated polar GaN(0001)-(1×1) surface is given in Fig. 6.49 [6.69]. The

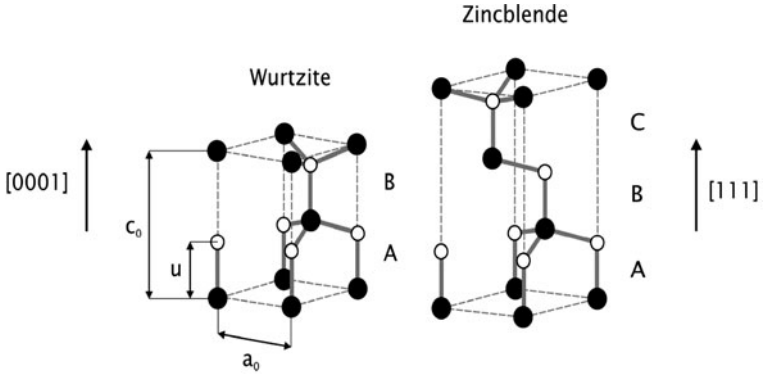

Fig. 6.47 Bulk atomic configuration of the hexagonal wurtzite and the cubic zincblende lattice. *Black* and *open circles* denote the two different types of atoms. Along the [0001] and the [111] directions the two structures differ in their stacking sequence ABAB... or ABCABC...

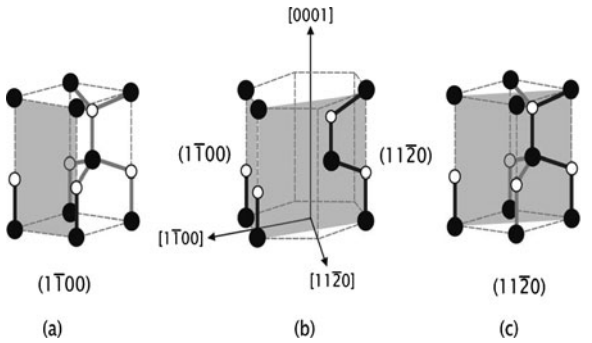

Fig. 6.48 Illustration of the different non-polar surfaces (1$\bar{1}$00) and (11$\bar{2}$0) of the hexagonal wurtzite lattice (*shaded planes*). (**a**) (1$\bar{1}$00) surface plotted into the smallest bulk unit cell. (**b**) (1$\bar{1}$00) and (11$\bar{2}$0) surfaces (*shaded*) plotted into the hexagonal unit cell. (**c**) (11$\bar{2}$0) surface plotted into the smallest bulk unit cell

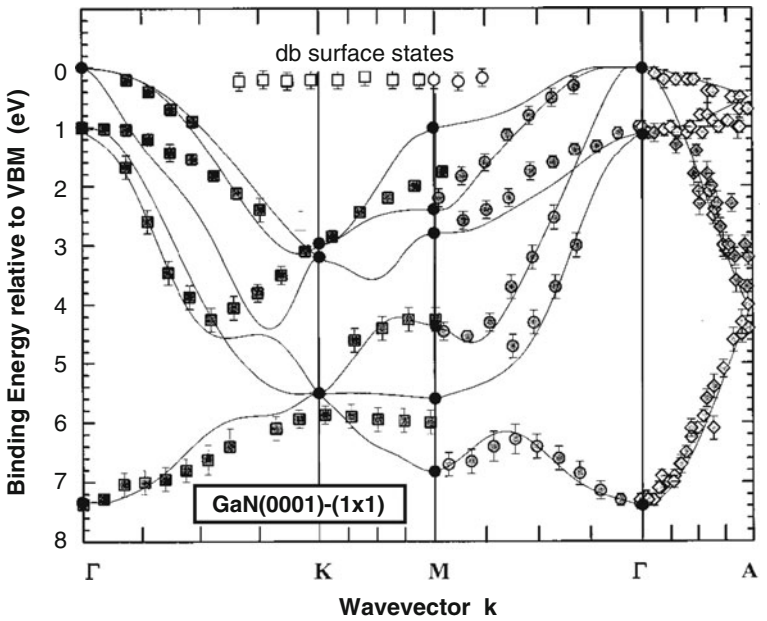

Fig. 6.49 Comparison of measured electronic band structure of GaN (data points according to Dhesi et al. [6.69]) and the calculation of Rubio et al. (*solid lines* [6.69]). The *open symbols* at energies near the valence band maximum (VBM) are not found in the bulk band structure and are attributed to dangling bond (db) surface states. The measurements have been performed on MBE-grown GaN(0001)-(1 × 1) surfaces

GaN layers were grown in plasma-assisted (for N production) MBE and the polar Ga-terminated Ga(0001)-(1 × 1) surfaces are prepared by several cleaning steps containing Ga deposition, annealing, and sputtering with N_2^+ ions [6.70]. Apart from the bulk band structure of GaN documented both by photoemission results (data points) and by band structure calculations (full lines) there is clear indication for a nearly dispersionless surface state band between the Γ, *K*, and *M* symmetry

points (Fig. 4.49) which is energetically located slightly below the Γ valence band maximum. The interpretation based on polarization measurements is given by the authors in terms of occupied dangling bond surface states with sp_z character derived from the Ga surface atoms. For the N-terminated GaN(000$\bar{1}$)-(1 × 1) surface prepared by Ar^+ ion sputtering and annealing a similar flat surface state band between Γ and K has been found in ARUPS near the Γ valence band maximum [6.71]. This has been attributed to the fact that large regions of the N polar surface are covered with an additional layer of Ga atoms bound at on-top positions above N atoms. A similarity with the occupied surface state band on GaAs(110) – even though a nonpolar surface – in Fig. 6.44 is obvious.

Meanwhile also experimental data for the nonpolar GaN surface are reported. In a detailed scanning tunneling microscopy/spectroscopy (X-STM/STS) study Bertelli et al. [6.72] could demonstrate that on freshly UHV cleaved nonpolar GaN(1$\bar{1}$00) surfaces of n-doped material the empty Ga-like and the filled N-like surface state bands are resonances at the Γ point of the Brillouin zone. This experimental result was also obtained theoretically by the authors from density functional theory (DFT) calculations and in an earlier publication by Northrup and Neugebauer [6.93]. Their results in Fig. 6.50 demonstrate that for the ideal (truncated bulk) Ga(10$\bar{1}$0) surface the Ga (S_{Ga}) and N (S_N) dangling bond surface state bands fall into bulk band gap along ΓM, while for the relaxed surface, similarly as on GaAs(110) (Fig. 6.44), the bands are shifted out of the bulk gap and become degenerate with the bulk conduction and valence bands at the Γ point. Note that the absolute band gap being about 3.4 eV for GaN is underestimated to about 2 eV in the DFT calculations of Fig. 6.50. This is a general property of non-advanced DFT calculations; nevertheless the general trends seen in Fig. 6.50 are realistic.

Similar experimental results for the intrinsic dangling bond N- and Ga-derived surface states on GaN(1$\bar{1}$00), namely their energetic location outside the fundamental band gap, were obtained from an STM study by Ivanova et al. [6.74]. The observed Fermi-level pinning position (Sect. 7.5) at about 1 eV below the conduction band edge was ascribed to extrinsic defect-derived surface states.

An extensive theoretical study on surface states on GaN and InN surfaces was performed by Van de Walle and Segev [6.75]. In contrast to the experimental findings an occupied Ga dangling bond surface state band is predicted near midgap, i.e., about 1.5 eV above the upper valence band edge on the GaN(0001) surface with (2 × 2) reconstruction. The difference between theory and the above-mentioned experimental results might be due to different types of surface reconstructions which are considered in theory and in experiment.

It is interesting that for the polar InN(0001)-(2 × 2) surface both occupied and empty In-derived dangling bond surface state bands are located above the lower conduction band edge of the absolute band gap (∼1.7 eV) as is seen in Fig. 6.51. This is in agreement with the general feature of narrow gap semiconductors (InAs, InSb, InN) that surface states are mainly derived from regions in reciprocal space, where the bulk density of states is high, i.e., from the side minima of the conduction band near the Brillouin zone boundary rather than from the energetically lower Γ minimum which determines the direct absolute gap.

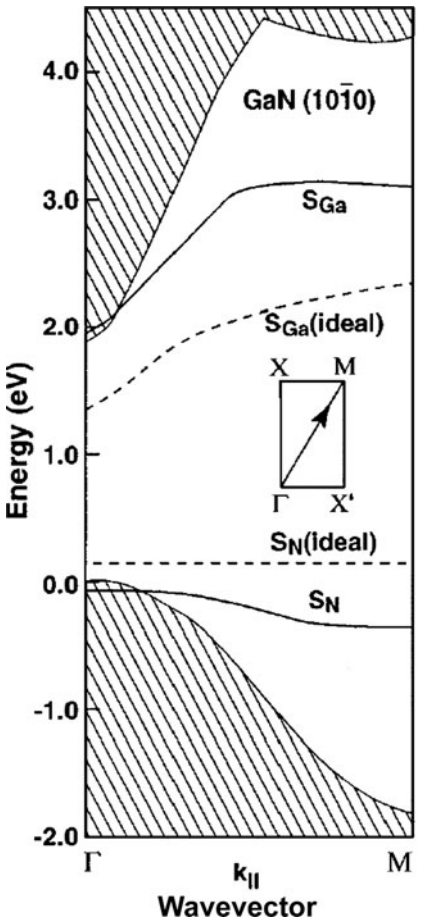

Fig. 6.50 Calculated surface state bands of the ideal (truncated bulk, in *broken line*) and the relaxed (in *solid line*) GaN(10$\bar{1}$0) surface along the Γ*M* direction in reciprocal space (inset). The empty upper bands are Ga derived (S_{Ga}), while the lower occupied bands are N-derived (S_N) dangling bond states. The shaded area is the projected bulk band structure. Note that the forbidden bulk gap is underestimated by more than 1 eV, a usual tendency in earlier density functional theory calculations without many body corrections [6.73]

In many practical cases III nitride layers are grown with [0001] orientation in plasma-assisted MBE under Ga-rich conditions because of better morphology. Under those conditions the (0001) surface is covered by a laterally contracted double layer of Ga [6.76]. At this high coverage the Ga–Ga bonding and dangling bond states that were distinct at moderate Ga/N ratios now strongly interact. This causes a strong dispersion of the corresponding surface state bands in the forbidden band and thus a broad density of states over the whole forbidden band, in the case of the narrow gap semiconductor InN even in the whole indirect gap (Fig. 6.52).

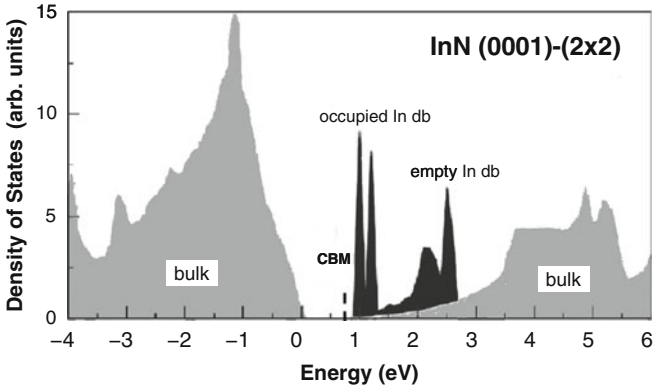

Fig. 6.51 Calculated density of states of the stable polar InN(0001)-(2 × 2) surface, which is found at moderate In/N ratios. Dark structures are surface state densities arising from occupied and empty In dangling bond (db) states; gray structures are due to bulk valence band ($E < 0$) and bulk conduction band states ($E > 0.7$ eV), i.e., above the conduction band minimum (CBM) [6.75]

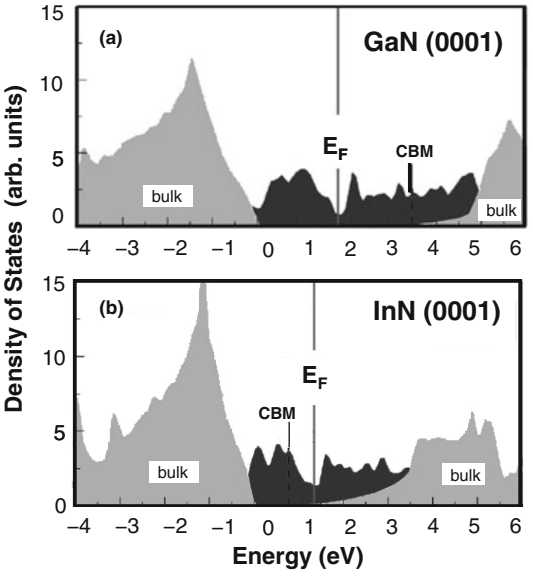

Fig. 6.52 Calculated densities of states of the stable polar (0001) surfaces of GaN (a) and InN (b) found under Ga- and In-rich conditions, respectively. The dark structures are due to surface states, while the gray structures are bulk valence ($E < 0$) and conduction band ($E >$CBM, conduction band minimum) [6.75]

6.5.4 II-VI Compound Semiconductors

Qualitatively, the trends in surface-state dispersion observed for III-V semiconductors are even more pronounced for the more ionic II-VI semiconductors. The best-studied example is ZnO with a direct bulk-band gap of 3.2 eV at 300 K. The main low-index surfaces are the polar (0001) Zn, $(000\bar{1})$O and the non-polar hexagonal $(10\bar{1}0)$ surface (Fig. 6.53). In Fig. 6.53 the sp^3-like bonding character – accom-

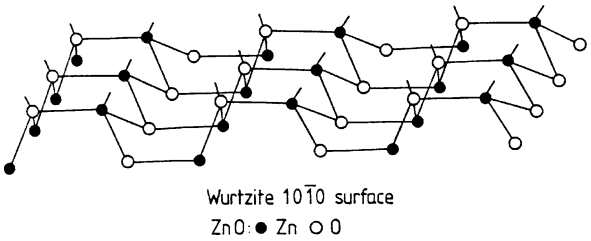

Fig. 6.53 Model of the non-polar wurtzite (10$\bar{1}$0) surface. For the example of ZnO, open circles might be attributed to oxygen and dark circles to Zn atoms

panying the strong ionic contribution – is clearly revealed from the essentially tetrahedral atom surrounding. All three surfaces can be prepared by cleavage in UHV. Comparing Fig. 6.43c,d with Fig. 6.53 one expects a similar reconstruction of the non-polar ZnO surface as found on GaAs(110). LEED intensity analyses indeed suggest a reconstruction in which the topmost oxygen atoms in Fig. 6.53 are shifted outwards, while the neighboring Zn atoms are displaced inwards. A detailed reconstruction model has been suggested in which the total vertical shifts (with respect to bulk) are: Δz (O) $= (-0.05 \pm 0.1)$ Å and Δz (Zn) $= (-0.45 \pm 0.1)$ Å, indicating a vertical contraction of the topmost Zn–O double-layer spacing with simultaneous dehybridization (i.e., shifts out of plane) of the O and Zn atoms in the uppermost plane. In principle, such a reconstruction should have a similar effect on the Zn (empty) and O (occupied) dangling-bond orbitals as in the case of GaAs(110). For the unreconstructed surface the Zn and O-derived dispersion branches should lie somewhere near the conduction-band E_C and valence-band E_V edge, respectively. This is indeed noted in the calculated band structure for the unreconstructed, truncated bulk-like (10$\bar{1}$0) surface (Fig. 6.54). The reconstruction which is found on real cleaved surfaces is expected to shift the unoccupied Zn band to higher, and the occupied O-derived band to lower energy; i.e., if the surface-band structure of Fig. 6.54 were correct in every detail for the unreconstructed surface,

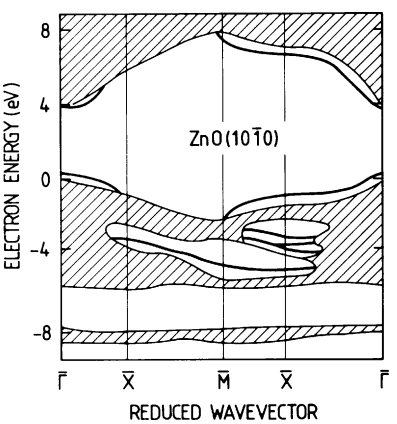

Fig. 6.54 Calculated surface state dispersion (solid lines) within the projected bulk state gaps for the non-polar ZnO(10$\bar{1}$0) surface. The projected bulk bands are shown as shaded areas. The symmetry point $\bar{X}$ of the 2D surface Brillouin zone lies perpendicular to the c-axis, $\bar{M}$ lies on the diagonal [6.67]

the reconstructed cleaved surface would have no dangling-bond surface states in the energy range of the band gap. There is indeed no indication from any experiment that the non-polar ZnO surface has intrinsic states in the forbidden band. Qualitatively, one might expect a weaker influence of the reconstruction on the surface-state band scheme than in the case of GaAs. Because of the high ionic bonding contribution in ZnO, the effect of reconstruction and even the presence of the surface (termination of the periodic potential) are relatively weak perturbations, as compared with the strong Coulomb forces. This also causes the close similarity between the bulk-band structure and surface states in Fig. 6.54, the surface states follow the bulk-band structure very closely. Experiment also supports this conclusion. The double differentiated EELS data (Panel IX: Chap. 4) in Fig. 6.55 measured on reconstructed ZnO surfaces prepared by cleavage in UHV are actually consistent with the band structure (Fig. 6.54) calculated for a non-reconstructed (1010) surface.

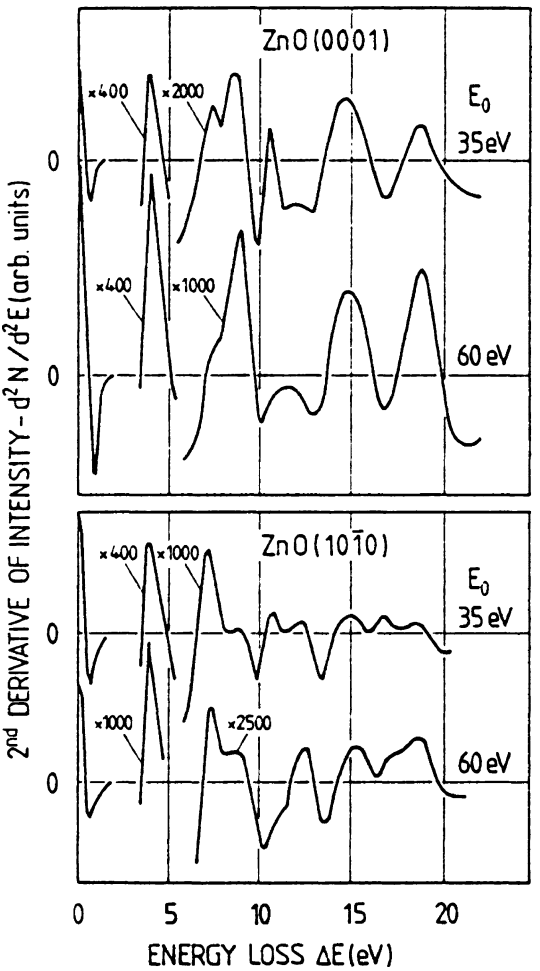

Fig. 6.55 Second derivative electron energy loss spectra measured on the clean polar Zn(0001) and the non-polar hexagonal (prism) (10$\bar{1}$0) surface with two different primary energies E_0. Magnification factors are with respect to the primary peak height [6.77]

Beside the bulk and surface-plasmon-like excitations near 19 and 15 eV, a number of peaks are observed due to electronic transitions at critical points of the bulk band structure. The strong transitions at 7.4 eV (on the non-polar surface) and at 11 eV (on both surfaces) are clearly due to surface states because of their characteristic dependence on primary energy E_0 (they are suppressed at higher E_0). The 7.4 eV transition obviously corresponds to excitations between occupied and empty dangling bond states from the flat $E(\boldsymbol{k}_\parallel)$ regions around $\overline{X}$ in Fig. 6.54. As is expected for a polar Zn surface, where only the Zn derived empty surface states are present, this transition is not observed in Fig. 6.55 (top); the weak structure near 7 eV is due to bulk transitions. The 11 eV transition probably originates from flat regions of the surface band structure at -4 eV near $\overline{X}$ in Fig. 6.54. Surface state transitions expected from Fig. 6.54 at around 4 eV from flat regions around $\overline{\Gamma}$ are likely to be contained in the strong loss feature at around 4 eV.

To conclude this chapter it should once more be emphasized that, on semiconductor surfaces in particular, the problem of atomic reconstruction is intimately connected with the dispersion of electronic surface states [6.68, 6.78]. A calculation of the 2D surface band structure is impossible without the detailed knowledge of the atomic positions on the surface. Conversely, examples discussed here show how important an experimental determination of the surface band structure is for establishing a correct structure model.

Panel XI
Photoemission and Inverse Photoemission

Photoemission [XI.1] and inverse photoemission spectroscopy [XI.2] are the most important experimental techniques for studying the band structure of occupied and empty electronic states, respectively. Depending on their kinetic energy the mean-free path of electrons in a solid ranges from about 5 Å up to some hundreds of Ångstroms. These techniques are therefore suited to studying both (3D) bulk and (2D) surface band structures $E(\boldsymbol{k})$ and $E(\boldsymbol{k}_\parallel)$, respectively. In particular, for photon energies below 100 eV the technique is highly surface sensitive and thus suitable for surface studies. *Photoemission Spectroscopy* (PS) performed with UV photons (UPS) or with X-ray photons (XPS) is based on the well-known photoelectric effect. The solid is irradiated by monochromatic photons which excite electrons from occupied states into empty states (within the solid), whence they are released into vacuum (free-electron plane-wave states) and detected by an electron-energy analyser. Thus the kinetic energy of the emitted photoelectron is determined and its wave vector $\boldsymbol{k}^{\mathrm{ex}}$ outside the solid is derived from its energy and the direction of the analyser aperture with respect to the sample orientation (Sect. 6.3). Since for the electron wave escaping from the crystal, the surface represents a 2D scattering potential (breakdown of translational symmetry), the wave vector $\boldsymbol{k}_\perp$ is not conserved; the internal $\boldsymbol{k}$ vector cannot be directly determined from the externally measured $\boldsymbol{k}^{\mathrm{ex}}$ (6.19–6.23) in Angle-Resolved UV Photoemission Spectroscopy (ARUPS). The basic relation for the photoemission process becomes clear from Fig. XI.1, where in the upper part schematic state densities of occupied and empty states (continuum above Fermi level E_{F}) are plotted. Optical excitation by a fixed photon energy $\hbar\omega$ populates empty states in the crystal above the vacuum level and the corresponding energy distribution of the electrons measured outside the crystal yields a qualitative image of the distribution of occupied crystal states (valence and core level states depending on the value of $\hbar\omega$). The measured distribution of sharp peaks is superimposed on the true secondary background, which arises from electrons that have lost quasi-continuous amounts of energy due to multiple scattering in the crystal (Sect. 6.3). The sharp peaks in the spectrum correspond to a kinetic energy E_{kin} of the externally detected electrons given by

$$E_{\mathrm{kin}} = \hbar\omega - E_{\mathrm{i}} - \phi, \tag{XI.1}$$

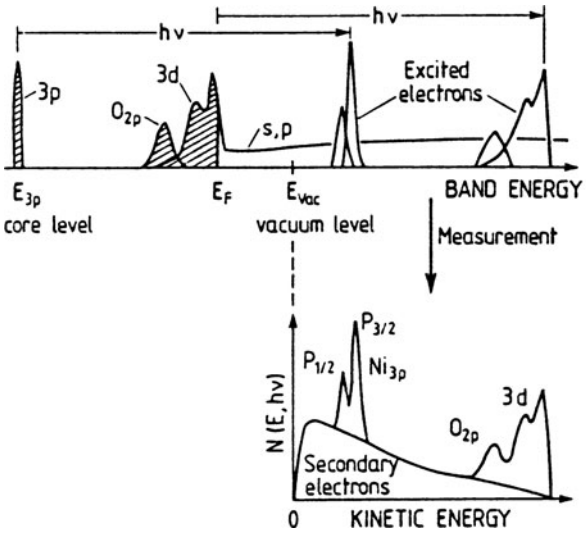

Fig. XI.1 Illustration of the photoemission process for the example of a transition metal surface (e.g., Ni) on which atomic oxygen (O $2p$) is adsorbed. Shadowed areas show occupied electronic states (up to the Fermi level E_F). Photons incident with energy $h\nu$ cause electrons to be excited into unoccupied quasi-continuous electron states within the crystal. These electrons can leave the crystal and are detected in the measurement as free electrons with a kinetic energy E_{kin}. Electrons that have undergone scattering processes on their way into vacuum are detected at lower energy and form a continuous background of so-called secondary electrons

where E_i is the binding energy of the initial state (to be determined) and ϕ the work function which has to be overcome by electrons reaching vacuum states. All energies in such a photoemission experiment are conveniently referred to the Fermi level E_F of the sample, since this energy is fixed (sample at earth or other fixed potential) and can be determined from the upper emission onset in the case of a metallic sample (or metallic overlayer).

The essential parts of the experimental set-up are a monochromatic light source, the sample contained in an UHV vessel to maintain clean surface conditions, and an electron energy analyser with detector. For angle-resolved measurements hemispherical or 127° deflectors (Panel II: Chap. 1) are used since they have a limited, well-defined acceptance angle. They allow the determination of $\boldsymbol{k}^{ex}$. When angular resolution is not required, cylindrical mirror analysers (Panel II: Chap. 1) can be employed. For the determination of densities of occupied states (integration over $\boldsymbol{k}^{ex}$) retarding field analysers collecting over a large acceptance angle are convenient.

As light sources for the UV range (UPS) gas discharge lamps are used; they are flanged to the UHV chamber through a differentially pumped capillary, which supplies the UV light to the sample surface (good windows for UV spectral range are not available). The lamp and capillary are pumped at several points, such that over a capillary diameter of about 1 mm a pressure gradient between 1 Torr (in the

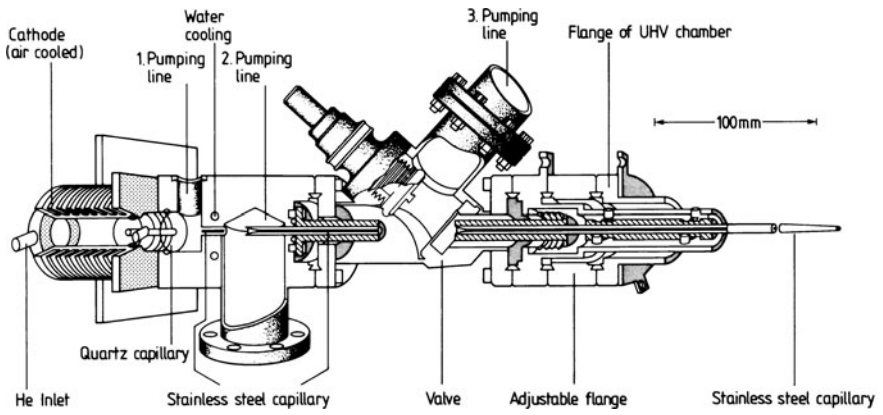

Fig. XI.2 Cross-sectional view of a UV discharge lamp for UV Photoemission Spectroscopy (UPS). The discharge quartz capillary is water cooled; three pump connections allow differential pumping; an UHV valve can interrupt the direct connection between discharge volume and UHV chamber

lamp) and $2 \cdot 10^{-10}$ Torr (in the UHV vessel) is sustained (Fig. XI.2). The discharge burns in a water- or air-cooled compartment, which is separated from the capillary by a UHV valve, allowing closure of the lamp without breaking the vacuum in the analysis chamber. Possible filling gases together with their main spectral emission lines are listed in Table XI.1. The most important source is the He discharge, where the He I spectral line ($\hbar\omega = 21.22$ eV), originating from excitations of the neutral He atom, is extremely intense, all other spectral lines giving rise to minor background only. This line is usually employed with no UV monochromator between lamp and sample. Depending on pressure (1 Torr for He I and 0.1 Torr for He II) and discharge current conditions the He II line at 40.82 eV can also be used without a monochromator. This emission originates from excited He^+ ions in the discharge.

In order to study core-level excitations, one requires higher photon energies as used in XPS (or ESCA). Conventional sources here are X-ray tubes whose characteristic emission lines (Table XI.1) are determined by the anode material (Fig. XI.3). Common anodes are composed of Mg or Al (Table XI.1). In addition, Y is an interesting anode material since it yields an emission line at 132.3 eV, just between the characteristic spectral ranges of UPS and XPS. The anodes of X-ray sources are water cooled in order to enhance the maximum emission intensity. The linewidths of the characteristic X-ray emission lines are several hundred meV (Table XI.1), such that fine-structure investigations or the analysis of chemical shifts, etc. are difficult if not impossible without the use of X-ray monochromators. Thus, for studies of core-level fine-structure, X-ray tubes are used in combination with an X-ray monochromator containing a crystalline mirror as a dispersive element (Fig. XI.4).

Nowadays synchrotron radiation has come to play a vital role in photoemission spectroscopy. A synchrotron yields a continuous spectrum of radiation extending from the far infrared to the hard X-ray regime. The cut-off depends on the acceleration energy (Fig. XI.5). Apart from the He I line of a discharge lamp its spectral

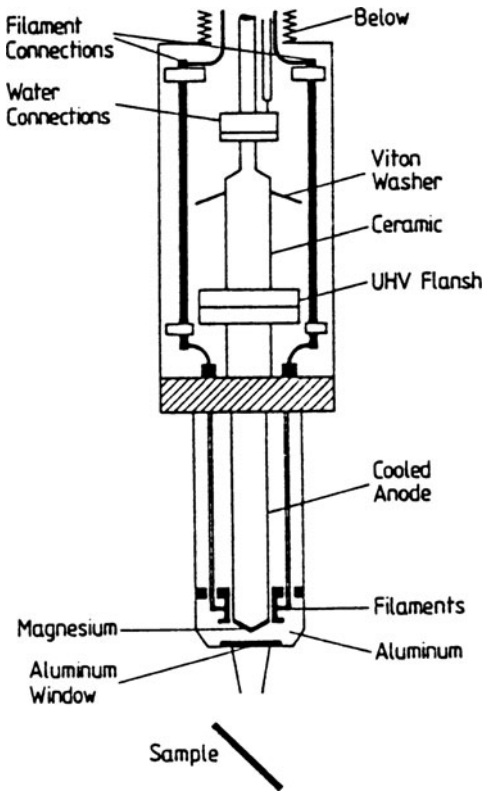

Fig. XI.3 Cross-sectional view of an X-ray source for X-ray Photoemission Spectroscopy (XPS). The anode, composed of either Mg or Al, is water cooled

emission intensity exceeds considerably that of all other discharge emission lines. UV and X-ray monochromators provide an adjustable spectral resolution for the experiments. Further advantages of synchrotron radiation are its 100% polarization in the plane of the ring, its high degree of collimation (1mrad $\times$ 1mrad typically), its high stability and well-defined time structure (light-house effect) for time-resolved experiments. Many experimental examples involving the application of photoemission spectroscopy are given in Chap. 6.

Inverse photoemission can be regarded as the time-reversed photoemission process [XI.5]. Electrons of well-defined energy are incident on the crystal, and are thereby injected into empty excited electronic states; from here they are deexcited into energetically lower empty states and the corresponding deexcitation energy is released as a photon (Fig. XI.6). Thus one measures the state of an extra electron injected into the solid. The energy of the unoccupied final state is given by the energy of the incident electron eU minus the energy of the detected photon $\hbar\omega$ (both referred to the experimentally determined Fermi level E_F). The theoretical description of the processes is similar to that of the normal photoemission process (three-step approximation, Sect. 6.3). Spectroscopy of unoccupied electronic states (above E_F) can be performed by varying the primary energy of the injected

Table XI.1 Commonly used line sources for photoelectron spectroscopy (UPS and XPS). In some cases (*) relative intensities of the lines depend on the conditions of the discharge. Values given are therefore only approximate. The data are compiled from several original sources [XI.1]

Source	Energy [eV]	Relative intensity	Typical intensity at the sample [photons/s]	Linewidth [meV]
He I	21.22	100	$1 \cdot 10^{12}$	3
Satellites	23.09, 23.75, 24.05	< 2 each		
He II	40.82	20*	$2 \cdot 10^{11}$	17
	48.38	2*		
Satellites	51.0, 52.32, 53.00	$< 1^*$ each		
Ne I	16.85 and 16.67	100	$8 \cdot 10^{11}$	
Ne II	26.9	20*		
	27.8	10*		
	30.5	3*		
Satellites	34.8, 37.5, 38.0	< 2 each		
Ar I	11.83	100	$6 \cdot 10^{11}$	
	11.62	80–40*		
Ar II	13.48	16*		
	13.30	10*		
YM_t	132.3	100	$3 \cdot 10^{11}$	450
$MgK_{\alpha 1,2}$	1253.6	100	$1 \cdot 10^{12}$	680
Satellites $K_{\alpha 3}$	1262.1	9		
$K_{\alpha 4}$	1263.7	5		
$AlK_{\alpha 1,2}$	1486.6	100	$1 \cdot 10^{12}$	830
Satellites $K_{\alpha 3}$	1496.3	7		
$K_{\alpha 4}$	1498.3	3		

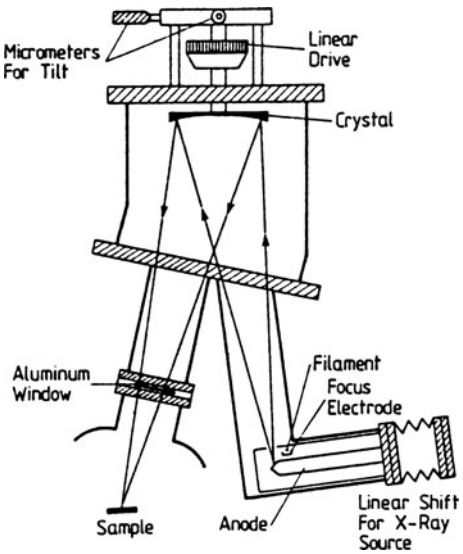

Fig. XI.4 Schematic of an X-ray monochromator for high-resolution XPS. The X-ray source is flanged to an UHV chamber containing a crystal mirror which acts, by means of Bragg reflection, as a dispersive element

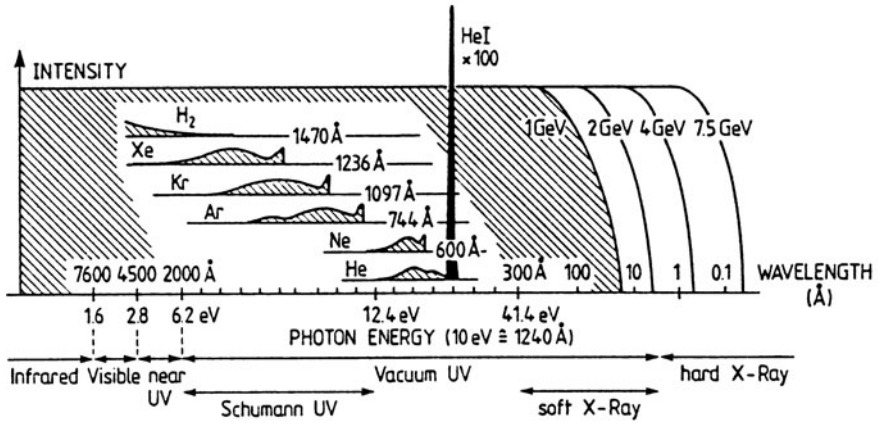

Fig. XI.5 Schematic comparison of the radiation spectrum emitted from a typical large synchrotron (e.g., DESY or BESSY) with that of classical discharge sources. Several particle energies (1 GeV up to 7.5 GeV) are indicated. The intensities all lie on roughly the same scale [XI.3, XI.4]

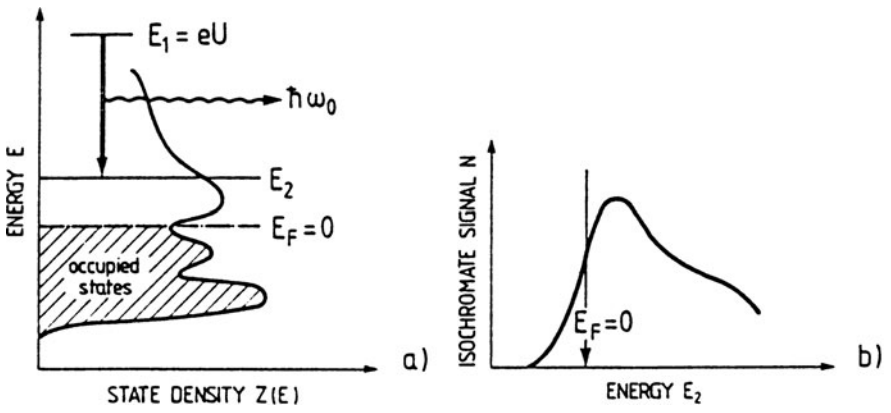

Fig. XI.6 (**a**) Schematic representation of the inverse photoemission process. An electron injected from outside the crystal enters an excited electronic state E_1 ($= eU$ if an external voltage U accelerates the electrons onto the sample); the electron is deexcited into a state E_2 and the corresponding energy is emitted as a photon of energy $\hbar\omega_0 = E_1 - E_2$. (**b**) Schematic isochromate spectrum $N(E_2) \propto Z(E_2)$ as obtained according to (**a**)

electrons and detecting photons of a well-defined fixed photon energy $\hbar\omega_0$ (within a fixed spectral window). This type of inverse photoemission spectroscopy is called *isochromate spectroscopy*. A second type of measurement uses a fixed electron energy in the primary beam and spectroscopic analysis of the emitted UV radiation by means of a UV spectrometer (*Bremsstrahlen spectroscopy*). The recorded UV spectrum (UV intensity versus photon energy) then directly yields a qualitative image of the distribution of unoccupied electronic states above E_F. Because of the involvement of electrons in this process the method is as surface sensitive as

photoemission spectroscopy. The distinction between bulk and surface electronic states is performed on an experimental basis as is done in UPS or XPS (Sect. 6.3). Angle-resolved inverse photoemission spectroscopy is possible by determining the wave vector of the injected electrons from their direction of incidence and their energy. Thus a mapping of the band structure $E(\boldsymbol{k})$ of unoccupied states – both 3D bulk and 2D interface states – becomes possible.

The experimental set-up in Bremsstrahlen spectroscopy consists of a high-intensity electron gun (necessary because of the low quantum yield of about 10^{-8} photons per electron) and a UV monochromator which is sometimes combined with modern multidetection units where typically 100 photon energies are recorded simultaneously with a channel plate amplifier and a position-sensitive resistive anode detector.

In isochromate spectroscopy the energy of the injected electrons is varied at the electron gun (Fig. XI.7) and the emitted UV photons are detected at a fixed energy by means of a Geiger counter equipped with a convenient band-pass filter window [XI.5, XI.6]. An elegant device consists of a Geiger counter filled with He ($\sim$ 500 mbar) and some iodine crystals; the counter is sealed with CaF_2 or SrF_2 windows (Fig. XI.7). The windows provide a high-energy cut-off for the UV radiation due to their characteristic absorption near 10.1 eV (CaF_2) or 9.7 eV (SrF_2), whereas the ionization of iodine (detection process)

$$I_2 + \hbar\omega \rightarrow I_2^+ + e^- \tag{XI.2}$$

starts at a photon energy of 9.23 eV and thus determines the low-energy cut-off for the photon detection. One thus has a band-pass detector for UV photons around 9.5 or 9.7 eV (Fig. XI.7). This fixed photon-energy detector can be made very efficient because of a large acceptance angle, but it has limited energy resolution. On the

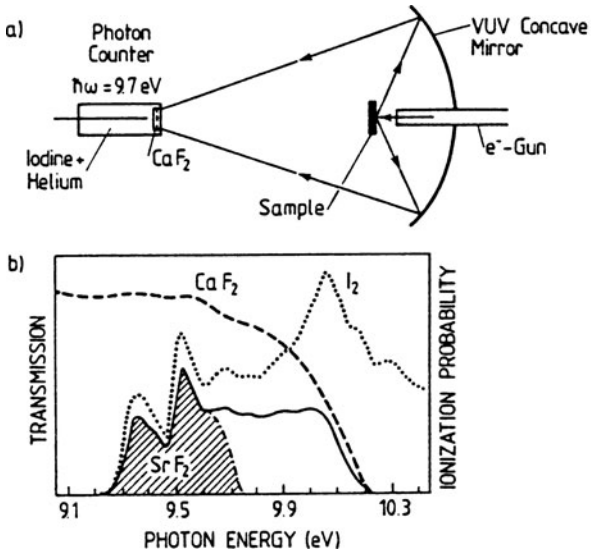

Fig. XI.7 (**a**) Inverse photoemission set-up using a Geiger counter (isochromate spectroscopy). The UV radiation emitted from the sample is focussed onto the window of a Geiger photon counter. (**b**) The spectral window of the detector is determined by the spectral transmittance of the counter window (SrF_2 or CaF_2) and by the spectral dependence of the ionization process of iodine [XI.5, XI.6]

other hand, in Bremsstrahlen spectroscopy the monochromator system achieves better energy resolution (0.3 eV) and can be tuned, but it is expensive and not as efficient in the case of low signal intensities.

As an example of the application of inverse photoemission spectroscopy in the study of metal-semiconductor interfaces, Fig. XI.8 depicts Bremsstrahlen spectra measured with an electron primary energy E_i of 15.3 eV (normal injection: $k_\parallel = 0$) on cleaved GaAs(110) surfaces covered with Pd overlayers of several thicknesses [XI.7]. The energy is referred to the upper valence band edge E_{VBM} such that the onset of emission from the unoccupied states due to the conduction band on the clean surface occurs at around 1.4 eV. The forbidden band of clean GaAs(110) surfaces is free of significant densities of empty states. With increasing Pd layer thickness a remarkable structure of empty interface states occurs in the band gap. As is seen from a comparison with the spectrum of the clean surface (dashed line) and from the difference spectra, the states in the conduction band range ($E > 1.4$ eV) are also modified due to the adsorbed Pd. A more detailed analysis of these results suggests that the interface states are due to d-like metal-derived levels. They are thought to be responsible for pinning the Fermi level E_F near midgap at such transition metal-semiconductor interfaces (Sect. 8.4).

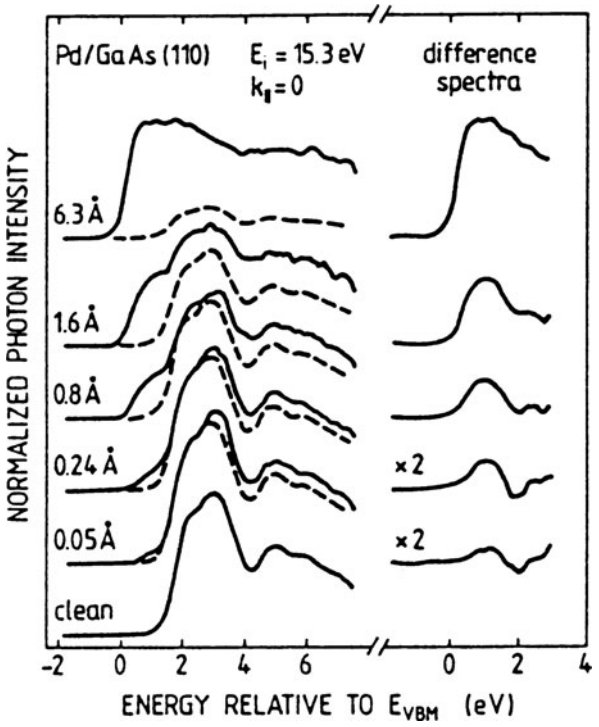

Fig. XI.8 Coverage-dependent inverse photoemission spectra (Bremsstrahlen spectra) spectra for Pd layers of different thickness (0.05–6.3) Å on GaAs(110). The raw data are shown together with difference curves which bring out the metal-induced interface states at about 1 eV above the valence band maximum. The clean surface spectrum is shown in each case by a dashed line [XI.7]

References

XI.1 M. Cardona, L. Ley (eds.): *Photoemission in Solids I, II*, Topics Appl. Phys., Vols. 26 and 27 (Springer, Berlin, Heidelberg 1978/79)
B. Feuerbacher, B. Fitton, R.F. Willis (eds.): *Photoemission and the Electronic Properties of Surfaces* (Wiley, New York 1978)
S. Hüfner: *Photoemission Spectroscopy, Principle and Applications*, 2nd edn., Springer Ser. Solid-State Sci., Vol. 82 (Springer, Berlin, Heidelberg 1996)
XI.2 V. Dose: Momentum-resolved inverse photoemission, Surf. Sci. Rep. **5**, 337-378 (1985)
XI.3 Y. Tanaka, A.S. Jursa, F.J. Le Blank: J. Opt. Soc. Am. **48**, 304 (1958)
XI.4 E.E. Koch: In Proc. 8th All Union Conf. High Energy Particle Physics, Erevan (1975), Vol. 2, p.502
XI.5 V. Dose: Appl. Phys. **14**, 117 (1977)
XI.6 A. Goldmann, M. Donath, W. Altmann, V. Dose: Phys. Rev. B **32**, 837 (1985)
XI.7 R. Ludeke, D. Straub, F.J. Himpsel, G. Landgren: J. Vac. Sci. Technol. A **4**, 874 (1986)

Problems

Problem 6.1 We may consider an Angle-Resolved UV Photoemission Spectroscopy (ARUPS) experiment where UV photons of energy 40.8 eV are incident on the (100) surface of a cubic transition metal with a work function of 4.5 eV. Photoemitted electrons from d states at 2.2 eV below the Fermi level are detected at an angle of 45° to the surface normal and in the [100] azimuth. Calculate the kinetic energy and the wave vector $\boldsymbol{k}$ of the emitted electrons. Describe the problem which arises in the derivation of the wave vector $\boldsymbol{k}_\mathrm{i}$ of the initial electronic states inside the crystal.

Problem 6.2 Treatment of the surfaces of n-doped ZnO with atomic hydrogen produces accumulation layers. Discuss charging character and possible origin of the responsible surface states.

Problem 6.3 Plot a qualitative picture of the shape of the π and π^* orbitals of surface states for the π-bonded chain model of the Si(111)-(2×1) surface (Sect. 6.5.1). By discussing the dipole matrix elements for the $\pi \rightarrow \pi^*$ optical transitions in a qualitative way show that optical absorption due to the transitions between the π and π^* surface-state bands can only be observed with light polarization parallel to the π-chains.

Problem 6.4

(a) For sufficiently small $\boldsymbol{k}_\parallel$ values the 2D-band of electronic surface states can be written in parabolic approximation as

$$E(\boldsymbol{k}_\parallel) = E_\mathrm{c} + \frac{\hbar^2}{2}\left(\frac{k_x^2}{m_x} + \frac{k_y^2}{m_y}\right)$$

with m_x and m_y as positive constants. Calculate the density of states $D^{(2\mathrm{D})}(E)$ around the critical point $E_\mathrm{c}(\boldsymbol{k}_\parallel = \boldsymbol{0})$ of the 2D band structure.

(b) Calculate the density of states in the neighborhood of a saddle point, where

$$E(\boldsymbol{k}_\parallel) = E_\mathrm{c} + \frac{\hbar^2}{2}\left(\frac{k_x^2}{m_x} - \frac{k_y^2}{m_y}\right)$$

with positive m_x, m_y.